1657 # Chapter 3 Climate Change From Short-Lived

1658 # Emissions Due to Human Activities

1659

1660 **Lead Author(s):** Drew T. Shindell, GISS/NASA; Hiram Levy II, GFDL/NOAA; Alice

1661 Gilliland, ARL/NOAA; M. Daniel Schwarzkopf, GFDL/NOAA; Larry W. Horowitz,

1662 GFDL/NOAA

1663

1664 **Contributing Authors:** Jean-Francois Lamarque, NCAR; Anne Waple, NCDC/NOAA

1665

1666 This chapter addresses the four questions regarding short-lived species that were posed in

1667 the Prospectus for this Report:

1668

1669 **Question 1**. What are the impacts of the radiatively active short-lived species not

1670 explicitly the subject of prior CCSP assessments (SAP 2.1a: Scenarios of Greenhouse

1671 Gas Emissions and Atmospheric Concentrations)?

1672

1673 **Answer 1**. Uncertainties in emissions projections for short-lived species are very large,

1674 even for a particular storyline. For aerosols, these uncertainties are usually dominant,

1675 while for tropospheric ozone, uncertainties in physical processes are more important.

1676 Differences among modeled future atmospheric burdens and radiative forcing for

1677 aerosols are dominated by divergent assumptions about emissions from South and East

1678 Asia. Aerosol mixing, aerosol indirect effects, the influence of ecosystem-chemistry

1679 interactions on methane, and stratosphere-troposphere exchange all contribute to large

1680 uncertainties separate from the emissions projections.

1681

1682 **Question 2**. How do the impacts of short-lived species compare with those of the well-

1683 mixed greenhouse gases as a function of the time horizon examined?

1684

1685 **Answer 2**. By 2050, two of the three models show a global mean annual average

1686 enhancement of the warming due to long-lived greenhouse gases by 20-25% due to the

1687 radiatively active short-lived species (which are not being reported in SAP 2.1). One

1688 model shows virtually no effect from short-lived species. To a large extent, the inter-

1689 model differences are related to differences in emissions. Short-lived species may play a

1690 substantial role relative to well-mixed greenhouse gases out to 2100. One model finds

1691 that short-lived species can contribute 40% of the projected summertime warming in the

1692 central US.

1693

1694 **Question 3**. How do the regional impacts of short-lived species compare with those of

1695 long-lived gases in or near polluted areas?

1696

1697 **Answer 3**. The spatial distribution of radiative forcing is generally less important than the

1698 spatial distribution of climate sensitivity in predicting climate impact. Thus, both short-

1699 lived and long-lived species appear to cause enhanced climate responses in the same

1700 regions of high climate sensitivity rather than short-lived species having an enhanced

1701 effect primarily in or near polluted areas.

1702

1703 **Question 4**. What might be the climate impacts of mitigation actions taken to reduce the

1704 atmospheric levels of short-lived species to address air quality issues?

1705

1706   **Answer 4**. Regional air quality emission control strategies for short-lived pollutants have

1707   the potential to substantially affect climate globally. Emissions reductions in the domestic

1708   sector in developing Asia, and to a lesser extent in the surface transportation sector in

1709   North America, appear to offer the greatest potential for substantial, simultaneous

1710   improvement in local air quality and mitigation of global climate change.

1711

1712   **3.1 Introduction**

1713   In this chapter, we describe results from numerical simulations of 21st century climate,

1714   with a major focus on the effects of short-lived gases and particulates. The calculations

1715   incorporate results from three different types of models:

1716

1717   1.   Integrated assessment models that produce emission scenarios for aerosols and for

1718   ozone and aerosol precursor species.

1719   2.   Global chemical composition models, which employ these emission scenarios to

1720   generate concentrations for the short-lived radiatively active species.

1721   3.   Global comprehensive climate models, which calculate the climate response to

1722   the projected concentrations of both the short-lived and long-lived species. Box

1723   1.1 outlines this sequence in detail.

1724

1725   The second part of Chapter 3, Section 3.2, is a discussion of the emission scenarios and

1726   the models used to generate them, and the chemical composition models (sometimes

1727   called chemical transport models) used to produce the global distributions of short-lived

1728   species that help to drive the comprehensive climate models. Section 3.2 shows that,

1729   beginning with a single socio-economic scenario for the time evolution of long-lived

1730   (well-mixed) greenhouse gases, different assumptions about the evolution of the aerosols

1731   and precursor species lead to very different estimates of aerosol and ozone concentrations

1732   for the 21st century. We conclude that uncertainties in emissions projections for short-

1733   lived species are very large, even for a particular storyline. For aerosols, these

1734   uncertainties are usually dominant, while for tropospheric ozone, uncertainties in physical

1735   processes are more important.

1736

1737   The third part of Chapter 3, Section 3.3, discusses the three global comprehensive climate

1738   models (Geophysical Fluid Dynamics Laboratory (GFDL); Goddard Institute for Space

1739   Studies (GISS); National Center for Atmospheric Research (NCAR)) that have been used

1740   used to calculate the impact of the short- and long-lived species[34] on the climate,

1741   focusing on the changes in surface temperature and precipitation. Supplementing the

1742   climate model results are calculations of the changes in radiative forcing[35] of the earth-

1743   atmosphere system. We find that by 2050, two of the three climate models show that

1744   radiatively active short-lived species enhance the global-mean annual-average warming

1745   due to long-lived greenhouse gases by 20-25%. One model shows virtually no effect from

1746   short-lived species. To a large extent, the inter-model differences are related to

1747   differences in emissions. One of the models has been extended to 2100. In that model,

---

[34] We distinguish here between short-lived species (which have atmospheric lifetimes less than one month and are non-uniformly distributed) and long-lived species (which have lifetimes of a decade or more and are generally well mixed in the atmosphere).

[35] Radiative forcing is defined in Section 3.3.3; briefly, it measures the net change in the energy balance of the earth-atmosphere system with space associated with a change in composition of any radiatively active species present in the atmosphere

1748   short-lived species play a substantial role, relative to the well-mixed greenhouse gases, in

1749   the surface temperature evolution out to 2100 and are responsible for 40% of the

1750   projected summertime warming in the central US.

1751

1752   The fourth part of Chapter 3, Section 3.4, discusses the effects of changes in regional

1753   aerosol and ozone and aerosol precursor emissions, using models that separate emissions

1754   by economic sector. The results show that regional air quality emission control strategies

1755   for short-lived pollutants have the potential to substantially affect climate at large-scales.

1756   Emission reductions from domestic sources in Asia, and to a lesser extent from surface

1757   transportation in North America, appear to offer the greatest potential for substantial,

1758   simultaneous improvement in local air quality and mitigation of global climate change.

1759

1760   **3.2 Emission Scenarios and Composition Model Descriptions**

1761   **3.2.1 Emission Scenarios**

1762   The long-lived (well-mixed) greenhouse gases included in this study were carbon dioxide

1763   (CO_2), nitrous oxide (N_2O), methane (CH_4), and the minor species (chlorofluorocarbons,

1764   sulfur hexafluoride). Projected global mean values were prescribed following the A1B

1765   'marker' scenario for all three modeling groups. Emissions for anthropogenic sources of

1766   aerosols and precursor species for all 3 composition model calculations were based on an

1767   international emission inventory maintained in the Netherlands (Olivier and Berdowski,

1768   2001).

1769

1770   Though the three groups in this study all prescribed future emissions following a specific

1771   socio-economic scenario (A1B) that was highly studied in the latest report by the

1772   Intergovernmental Panel on Climate Change (IPCC), they used different emissions trends

1773   for the short-lived species. There are several reasons for the differences. For one, the

1774   A1B emissions projections only provide estimates of anthropogenic emissions, and each

1775   model used its own natural emissions (though these were largely held constant).

1776   Secondly, integrated assessment models, while using the same socio-economic storyline

1777   (A1B), provided a range of emission results (Nakicenovic *et al.*, 2000).

1778

1779   Two groups, GFDL and NCAR, used output from the AIM integrated assessment model

1780   (integrated assessment models are defined in Chapter 2, Section 2.1) while GISS used

1781   results from the IMAGE model. Though the emissions output generated from AIM was

1782   denoted the 'marker' scenario by the IPCC, it was noted that it did not represent the

1783   average, best, or median result, and that all integrated assessment model results should be

1784   treated equally. Finally, emissions for some species, such as carbonaceous aerosols, were

1785   not provided. This last issue motivated the GISS choice of the IMAGE model output, as

1786   it provided sufficient regional detail to allow carbonaceous aerosol emissions to be

1787   estimated consistently with the other species. Another complexity was the treatment of

1788   biomass burning emissions, which are partly natural and partly anthropogenic. In the

1789   GFDL model, biomass-burning emissions were assumed to be half-anthropogenic and

1790   half natural. The GISS model instead used biomass burning emissions projections from

1791   another inventory (Streets *et al.*, 2004).

1792

1793   The result is a substantial divergence in the projected trends among the three models

1794   (Figure 3.1, Table 3.1). For sulfur dioxide (SO_2), the precursor to sulfate aerosol, the

1795   emissions follow reasonably similar trajectories, with globally averaged increases until

1796   2030 followed by decreases to 2050 and even further decreases to 2100. However, the

1797   percentage increase is roughly double for GISS and NCAR as compared with GFDL.

1798   Thus even two composition models using anthropogenic emission projections from the

1799   same integrated assessment model show large differences in the evolution of their total

1800   emissions, presumably owing to differences in the present-day emission inventories . At

1801   2050, the GFDL model has substantially reduced emissions compared with 2000, while

1802   the other models show enhanced emissions relative to 2000. A similar divergence in

1803   projected sulfur-dioxide trends is present in the 2.1a stabilization emission scenarios

1804   discussed in Chapter 2, with emissions decreasing dramatically (~70%) by 2050 in one

1805   integrated assessment model (MINICAM) while decreasing only moderately (~20%) in

1806   the two others, and even beginning to increase again after about 2040 in one of those two.

1807

1808   Differences are even more striking for carbonaceous aerosols emissions, which were not

1809   provided by any of the integrated assessment models. We focus on black carbon (BC) as

1810   the more important radiative perturbation. For this aerosol (and for organic carbon(OC)),

1811   the GFDL composition model uses the IPCC recommendation to scale carbonaceous

1812   aerosol emissions to carbon monoxide emissions, leading to substantial increases with

1813   time (Figure 3.1, Table 3.1). However, many of the sources of carbon monoxide emission

1814   are different from those of carbonaceous aerosols. The NCAR group did not simulate the

1815   future composition of black and organic carbon based on emission projections, but

1816   instead scaled their present-day distribution by the global factors derived for sulfur

1817   dioxide. The time evolution of black and organic carbon emissions in the NCAR model

1818   thus follows the same trajectory as that of SO_2. On the other hand, the GISS group used

1819   emissions projections from (Streets *et al.*, 2004) based on energy and fuel usage trends

1820   from the IMAGE model (as for other species) and including expected changes in

1821   technology. This led to a substantial reduction in future emissions of carbonaceous

1822   aerosols.

1823

1824   For precursors of tropospheric ozone, there was again divergence among the models. The

1825   primary precursor in most regions, NO_x (nitrogen oxides = $NO + NO_2$), increased steadily

1826   in the projections used by GISS, while it peaked at 2030 and decreased slightly thereafter

1827   in the projections used at GFDL (Table 3.1). Hydrocarbons and carbon monoxide show

1828   analogous differences. Methane was prescribed according to the A1B "marker" scenario

1829   values for all three composition models. Thus ozone, in addition to the aerosols, was

1830   modeled in substantially different ways at the three centers.

1831

1832   The three models included projected changes in the same species, with the exception of

1833   nitrate, which only varied in the GISS model. As its contribution to total aerosol and total

1834   aerosol radiative forcing is small, at least in this GISS model, this particular difference

1835   was not significant in our results.

1836 **Table 3.1. Global Emissions. Emissions include both natural and anthropogenic sources. Values in**
1837 **parentheses are changes relative to 2000.**

Species	Model	2000	2030	2050	2100
NO_x (Tg N/yr)	GFDL	40	57 (43%)	54 (35%)	48 (20%)
	GISS	50.5	67.0 (33%)	77.5 (53%)	NA
BC (Tg C/yr)	GFDL	10.9	14.0 (28%)	15.3 (40%)	19.9 (83%)
	GISS	8.6	6.8 (-21%)	6.0 (-30%)	NA
OC (Tg C/yr)	GFDL	51.5	61.9 (20%)	66.5 (29%)	84.3 (%)
	GISS	69.5	57.0 (-18%)	58.3 (-16%)	NA
SO_2 (Tg SO_2/yr)	GFDL	147	187 (27%)	118 (-20%)	56 (-62%)
	GISS	130	202 (55%)	164 (26%)	NA
	NCAR	125	190 (52%)	148 (18%)	NA
Dust (Tg/yr)	GFDL	2471	2471	2471	2471
	GISS	1580	1580	1580	NA

1838

1839 **3.2.2 Composition Models**

1840 The chemical composition models used to produce short-lived species concentrations for

1841 the GFDL, GISS, and NCAR climate models were driven by the emissions projections

1842 discussed in Section 3.2.1. While the three models did not use identical present-day

1843 emissions, their anthropogenic emissions were based on the same international inventory

1844 (Olivier and Berdowski, 2001). The chemical composition simulations were run for one

1845 or two years, with the three-dimensional monthly mean concentrations and optical

1846 properties archived for use as off-line concentration fields to drive the climate model

1847 simulations discussed in Section 3.3. These simulations were all performed with present-

1848 day meteorology (values for temperature, moisture, and wind). Further details about the

1849 chemical composition models are provided in Appendix 1.

1850
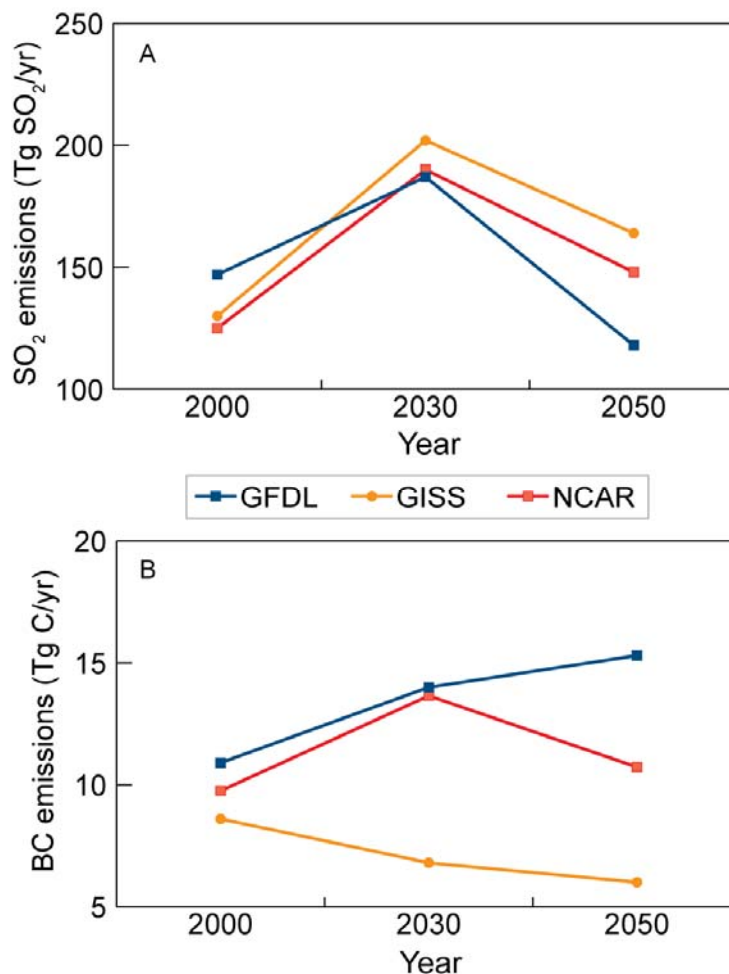
1851
1852
1853 **Figure 3.1** A1B emissions trends used in the three models for SO_2 (top) and BC (bottom). Note that in the
1854 NCAR model, the present day black carbon distribution was scaled in the future rather than calculated from
1855 BC emissions. Scaling was chosen to mimic the global sulfur dioxide emissions, a 40% increase over 2000
1856 at 2030, and 10% at 2050. The NCAR 2000 black carbon global emission is set at the average of the GISS
1857 and GFDL 2000 values, and follows this scaling in the future, for illustrative purposes**.**
1858

1859 **3.2.2.1 Geophysical Fluid Dynamics Laboratory (GFDL)**

1860 Composition changes for the short-lived species in the GFDL experiments were

1861 calculated using the global chemical transport model MOZART-2 (Model for OZone

1862 And Related chemical Tracers, version 2.4), which has been described in detail

1863 previously (Horowitz *et al.*, 2003; Horowitz, 2006; and references therein). This model

1864 was used to generate the monthly average distributions of tropospheric ozone, sulfate,

1865 and black and organic carbon as a function of latitude, longitude, altitude, and time for

1866   the emission scenarios discussed above. Simulated ozone concentrations agree well with

1867   present-day observations and recent trends (Horowitz, 2006). Overall, the predicted

1868   concentrations of aerosol are within a factor of two of the observed values and have a

1869   tendency to be overestimated (Ginoux *et al.*, 2006). Further details on the MOZART

1870   model are found in Appendix 3.1, in the section on Geophysical Fluid Dynamics

1871   Laboratory.

1872

1873   **3.2.2.2 Goddard Institute for Space Studies (GISS)**

1874   The configuration of the GISS composition model used here has been described in detail

1875   in (Shindell *et al.*, 2007). In brief, the composition model PUCCINI (Physical

1876   Understanding of Composition-Climate INteractions and Impacts) includes ozone and

1877   oxidant photochemistry in both the troposphere and stratosphere (Shindell *et al.*, 2006b),

1878   sulfate, carbonaceous and sea-salt aerosols (Koch *et al.*, 2006, 2007), nitrate aerosols

1879   (Bauer *et al.*, 2006), and mineral dust (Miller *et al.*, 2006a). Present-day composition

1880   results in the model are generally similar to those in the underlying chemistry and aerosol

1881   models. Further details on the PUCCINI model resolution, composition, and performance

1882   are found in Appendix 3.1, in the section on Goddard Institute for Space Studies.

1883

1884   **3.2.2.3 National Center for Atmospheric Research (NCAR)**

1885   For the climate simulations described in this section, present-day tropospheric ozone was

1886   taken from (Lamarque *et al.*, 2005a); beyond 2000, tropospheric ozone was calculated by

1887   T. Wigley using the MAGICC composition model

1888   (http://www.cru.uea.ac.uk/~mikeh/software/magicc.htm) forced by the time-varying

1889   emissions of NO_x, methane and volatile organic compounds (VOCs) and these average

1890   global values were used to scale the present-day distribution. Future carbonaceous

1891   aerosols are scaled from their present-day distribution (Collins *et al.*, 2001) by a globally

1892   uniform factor whose time evolution follows the global evolution of SO_2 emissions.

1893   Stratospheric ozone changes are prescribed following the study by (Kiehl *et al.*, 1999).

1894   Further details on the composition models used by NCAR are found in Appendix 3.1 in

1895   the section on National Center for Atmospheric Research.

1896

1897   **3.2.3 Tropospheric Burden**

1898   The composition models each calculate time-varying three-dimensional distributions of

1899   the short-lived species (except for NCAR where 2030 and 2050 ozone, black carbon, and

1900   organic carbon were scaled based on their 2000 distributions). We compare these using

1901   the simple metric of the global mean annual average tropospheric burden (*i.e.* the total

1902   mass in the troposphere). As was the case with emissions, the differences between the

1903   outputs of the composition models are substantial (Table 3.2). The GFDL model has a

1904   67% greater present-day burden of sulfate than the GISS model, for example. As the

1905   GFDL sulfur dioxide emissions were only 13% greater, this suggests that either sulfate

1906   stays in the air longer in the GFDL model than in the GISS model or sulfur dioxide is

1907   converted more efficiently to sulfate in the GFDL model.

1908   **Table 3.2 Global Burdens.** Values in parentheses are changes relative to 2000.

Species	Model	2000	2030	2050	2100
BC (Tg C)	GFDL	0.28	0.36 (29%)	0.39 (39%)	0.51
	GISS	0.26	0.19 (-27%)	0.15 (-42%)	NA
	NCAR		(40%)	(10%)	
OC[*] (Tg C)	GFDL	1.35	1.59 (18%)	1.70 (26%)	2.15
	GISS	1.65	1.33 (-19%)	1.27 (-23%)	NA
	NCAR		(40%)	(10%)	
Sulfate (Tg $SO_4^=$)	GFDL	2.52	3.21 (27%)	2.48 (-2%)	1.50 (-40%)
	GISS[**]	1.51	2.01 (33%)	1.76 (17%)	NA
	NCAR				
Dust (Tg)	GFDL	22.31	22.31	22.31	22.31
	GISS	34.84	34.84	34.84	NA
	NCAR				
Tropospheric Ozone (DU)	GFDL	34.0	38.4 (+13%)	39.3 (+16%)	38.2 (+12%)
	GISS	31.6	41.5 (31%)	47.8 (51%)	NA
	NCAR	28.0	41.5 (48%)	43.0 (54%)	NA

1909   [*]The organic carbon (OC) burdens include primary OC aerosols (with emissions as in above table) plus
1910   secondary OC aerosols (SOA). In the GFDL model, the global burden of SOA is 0.07 Tg C in this
1911   inventory. In the GISS model, organic carbon from SOA makes up ~24% of present-day OC emissions.
1912   [**]GISS sulfate burdens include sulfate on dust surfaces, which makes up as much as ½ the total burden.
1913

1914   This can be tested by analyzing the atmospheric residence times of the respective models

1915   (Table 3.3). The residence time of sulfate is within ~10% in the two models, and in fact is

1916   slightly less in the GFDL model. This indicates that the conversion of sulfur dioxide

1917   (SO_2) to sulfate must be much more efficient in the GFDL model for it to have a sulfate

1918   burden so much larger than the GISS model. This is clearly seen in the ratio between

1919   sulfate burden and SO_2 emissions (Table 3.4). This ratio can be analyzed in terms of the

1920   total sulfur dioxide burden (in Tg) per SO_2 emission (in Tg/yr); the change in SO_2 burden

1921   per SO_2 emission change, or alternatively in the percentage change in each. The latter is

1922   probably the most useful evaluation, as the fractional change will reduce differences

1923   between the starting points of the two models. We note that this metric is affected by both

1924   production and removal rates in the models. Table 3.4 shows clearly that the production

1925   of sulfate per Tg of sulfur emitted is much greater in the GFDL model than in the GISS

1926   model, either because of differences in other sources of sulfate (*e.g.*, from dimethyl

1927   sulfate (DMS)) or difference in the chemical conversion efficiency of SO_2 to sulfate

1928   (versus physical removal of SO_2 by deposition).

1929
1930   **Table 3.3 Global mean annual average aerosol residence times (days)**

Species	Model	2000	2030	2050
BC	GFDL	9.4	9.4	9.3
	GISS	11.0	10.2	9.1
OC	GFDL	9.6	9.4	9.3
	GISS	8.7	8.5	8.0
Sulfate	GFDL	8.0	8.2	8.1
	GISS	8.8	8.8	9.0

1931

1932   The residence times of black and organic carbon (BC and OC) are also fairly similar in

1933   these two models (Table 3.3). While the concentrations of sulfate and carbonaceous

1934   aerosols are all influenced by differences in how the models simulate removal by the

1935   hydrologic cycle, accounting for at least some of the 10-15% difference in residence

1936   times, sulfate production can vary even more from model to model, as its production

1937   from the emitted sulfur dioxide involves chemical oxidation, which can differ

1938   substantially between models. Removal of sulfur dioxide prior to conversion to sulfate

1939   may also be more efficient in the GISS model. In contrast, BC and OC are emitted

1940   directly, and hence any differences in how these are represented in the models would be

1941   apparent in their residence times.

1942 **Table 3.4 Ratio of sulfate and ozone burdens to precursor emissions, global mean annual average**

Species	Model	2000 Tg burden/ Tg emission	2030 vs. 2000 Tg burden/ Tg emission	2030 vs. 2000 % burden/ % emission	2050 vs. 2000 % burden/ % emission
Sulfate	GFDL	0.017	0.017	1.00	0.08[*]
	GISS	0.012	0.007	0.60	0.65
Ozone	GFDL	7.19	2.24	0.32	0.44
	GISS	6.82	6.54	0.94	0.96

1943   Ratios for sulfate are in Tg sulfate per Tg S/yr SO_2 emitted. Ozone ratios are in Tg ozone per Tg N/yr NO_x
1944   emitted. Ozone values in Table 3.2 are converted to burden assuming 1 DU globally averaged = 10.9 Tg
1945   ozone.
1946   [*]The burden change was only 2% in this case, making the calculation unreliable.
1947
1948   The aerosol residence times are relatively stable in time in the GISS and GFDL models.

1949   The carbonaceous aerosol residence times do decrease with time in the GISS model (and

1950   to a lesser extent in the GFDL model for OC), probably owing to the shift with time from

1951   mid to tropical latitudes, where wet and dry removal rates are different (more rapid net

1952   removal). The sulfate residence time is fairly stable over the 2000 to 2050 period. The

1953   ratio of sulfate burden to SO_2 emissions is the same for the present-day and the 2030 to

1954   2000 changes in the GFDL model. For the 2100 to 2000 change in that model (not

1955   shown), the ratio drops from 1.00 to 0.65. As the total emissions of SO_2 decrease, a larger

1956   fraction of the sulfate production comes from DMS oxidation rather than from emitted

1957 SO_2. The conversion efficiency from SO_2 to sulfate also varies over time in the GISS

1958   model, decreasing to 2030 and increasing thereafter (inversely related to total sulfur

1959   dioxide emissions). This may reflect both non-linearities in production (via oxidation

1960   chemistry) and the changing spatial pattern of emissions.

1961

1962   After comparison of the inter-model variations in aerosol residence times and chemical

1963   conversion efficiencies with the variations in emissions trends, it is clear that the

1964   differences in the projected changes in aerosol burdens in the GISS and GFDL

1965   simulations are primarily attributable to the underlying differences in emissions. This is

1966   especially true for carbonaceous aerosols, for which the residence times are quite similar

1967   in the models. Even though there is a greater difference in sulfate burdens due to the

1968   variations in chemical conversion efficiency between the models, the emissions trends at

1969   2050 relative to 2000 are of opposite sign in the two models and thus dominate the

1970   difference in the burden change. Thus, the GISS model projects a greater sulfate burden

1971   at 2050 than at 2000, but substantially reduced burdens of carbonaceous aerosols, while

1972   the GFDL model projects the opposite, both because of the underlying emissions

1973   projections.

1974

1975   The results for tropospheric ozone tell a different story. The ozone burden increases in

1976   the future in all three models, but the percentage increase relative to 2000 differs by more

1977   than a factor of three at 2030 (Table 3.2). Examining the ozone changes relative to the

1978 NO_x emissions changes, there are very large differences between the GFDL and GISS

1979   models (Table 3.4). This may reflect the influence of processes such as stratospheric

1980   ozone influx which are independent of NO_x emissions, as well as the roles of precursors

1981   such as carbon monoxide (CO) and hydrocarbons that also influence tropospheric ozone.

1982   In particular, the GISS model computed a large increase in the flux of ozone into the

1983   troposphere as the stratospheric ozone layer recovered, while the composition model used

1984   at GFDL to calculate ozone held stratospheric ozone fixed and hence did not simulate

1985   similar large increases. In addition, there are well-known non-linearities in O_3-NO_x

1986   chemistry (Stewart *et al.*, 1977), and it has been shown that the ozone production

1987   efficiency can vary substantially with time (Lamarque *et al.*, 2005a; Shindell *et al.*,

1988   2006a). Thus for tropospheric ozone, the differences in modeled changes of nearly a

1989   factor of three (13 vs. 33% increase) are much larger than the differences in the NO_x

1990   precursor emissions (33 vs. 43% increase).

1991

1992   **3.2.4 Aerosol Optical Depth**

1993   The global mean present-day all-sky aerosol optical depth (AOD)[36] in the three models

1994   ranges from 0.12-0.20 (Table 3.5). This difference of almost a factor of 2 suggests that

1995   aerosols are contributing quite differently to the Earth's energy balance with space in

1996   these models. Observational constraints on the all-sky value are not readily available, as

1997   most of the extant measurement techniques are reliable only in clear-sky (cloud-free)

1998   conditions. Sampling clear-sky areas only, the GISS model's global total aerosol optical

1999   depth is 0.12 for 2000 (0.13 Northern Hemisphere, 0.10 Southern Hemisphere). This

2000   includes contributions from sulfate, carbonaceous, nitrate, dust, and sea-salt aerosols. The

2001   clear-sky observations give global mean values of ~0.135 (ground-based AERONET) or

2002   ~0.15 (satellite composites, including AVHRR or MODIS observations), though these

2003   have substantial limitations in their spatial and temporal coverage. The NCAR and GFDL

2004   models did not calculate clear-sky aerosol optical depth. Given that the all-sky values are

2005   larger, and substantially so in the GISS model (though this will depend upon the water

2006   uptake of aerosols), it seems clear that the values for NCAR would be too small

2007   compared with observations since even their all-sky values are lower than the estimate

2008   from observations. This may be related to NCAR's use of AVHRR data in assimilation of

---

[36] Aerosol optical depth is a measure of the fraction of radiation at a given wavelength absorbed or
scattered by aerosols while passing through the atmosphere.

2009   aerosol optical depth to create the NCAR climatology *(*Collins *et al.*, 2001, 2006), as that

2010   data appears to be low relative to MODIS observations, for example.

2011

2012   For all three models, there are large differences in the contributions of the various aerosol

2013   species (Figure 3.2, Table 3.5). This is true even for GFDL and GISS models, with

2014   relatively similar all-sky global mean aerosol optical depths. More than half the aerosol

2015   optical depth in the GFDL model comes from sulfate, while this species contributes only

2016   about 1/8th the aerosol optical depth in the GISS model. Instead, the GISS model's

2017   aerosol optical depth is dominated by the largely natural sea-salt and dust aerosols, which

2018   together contribute 0.14 to the aerosol optical depth. These two species contribute a much

2019   smaller aerosol optical depth in the NCAR and GFDL models, ~0.06 or less, with the

2020   differences with respect to GISS predominantly due to sea-salt. The relative contribution

2021   from sulfate in the NCAR model looks similar to the GFDL model, with nearly half its

2022   aerosol optical depth coming from sulfate, but the magnitude is much smaller. It seems

2023   clear that the GFDL model's direct sulfate contribution is biased high (Ginoux *et al.*,

2024   2006), while the GISS model's sulfate is biased low in this model version (Shindell *et al.*,

2025   2007). However, the relative importance of the different aerosols species is not well

2026   understood at present (Kinne *et al.*, 2006).

2027
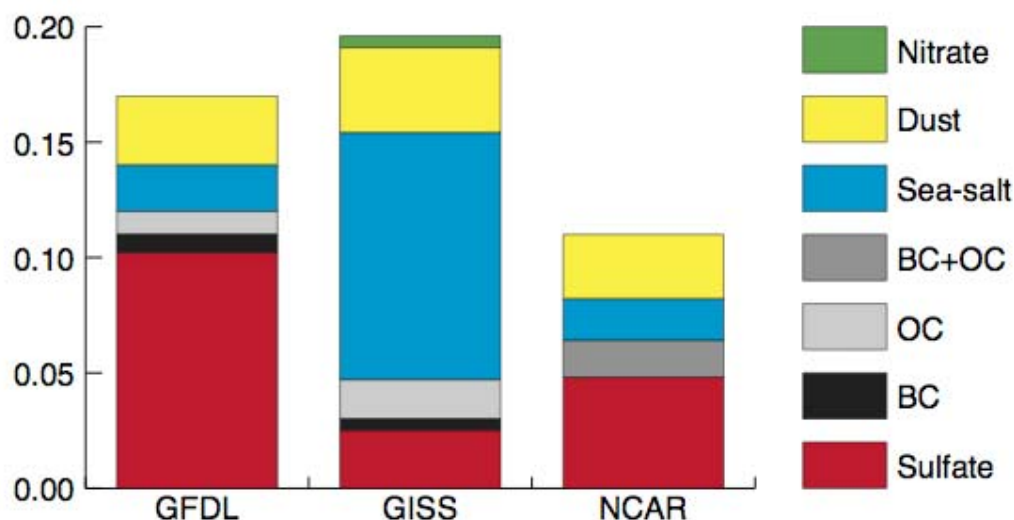
Figure 3.2 Present-day contributions from individual aerosol species to global mean all-sky aerosol optical depth (550 nm extinction). Neither GFDL nor NCAR include nitrate.

Large differences in the relative aerosol optical depth in the Northern Hemisphere and

Southern Hemisphere are also apparent in the models (Table 3.5). The ratios of the

present-day Northern Hemisphere to Southern Hemisphere total aerosol optical depths in

the three models differ widely, with values of 2.43, 1.97, and 0.96 in the GFDL, NCAR,

and GISS models, respectively. This clearly reflects the dominant contribution of sulfate

to optical depth in the GFDL and NCAR models, as this species has large anthropogenic

Northern Hemisphere sources, and the dominance of sea-salt in the GISS model, with its

largest source being the Southern Ocean. While composite satellite data shows clearly

greater aerosol optical depths in the Northern Hemisphere than the Southern Hemisphere,

most satellite instruments lose coverage near the northern edge of the Southern Ocean

(Kinne *et al.*, 2006). Unfortunately, quality-controlled networks such as AERONET

provide virtually no ground-based data poleward of 45°S. Thus while it seems unlikely

that the aerosol optical depth is larger in the Southern Hemisphere than the Northern

Hemisphere, as in the GISS model, presently available data are not adequate to fully

2046   characterize this ratio, as aerosol optical depths over the Southern Ocean are poorly

2047   known.

2048   **Table 3.5 Aerosol optical depth (550nm extinction) – ALL-SKY**

Region	aerosol type	Model	2000	2030	2050	2100
Global	BC	GFDL	.0076	.0096	.0105	.0138
		GISS	.0045	.0034	.0028	NA
	Sulfate	GFDL	.1018	.1227	.0906	.0591
		GISS	.0250	.0312	.0278	NA
		NCAR	.048	.062	.052	NA
	Sea-salt	GFDL	.0236	.0236	.0236	.0236
		GISS	.1065	.1080	.1050	
		NCAR	.018	.018	.018	NA
	Dust	GFDL	.0281	.0281	.0281	.0281
		GISS	.0372	.0389	.0387	
		NCAR	.0275	.0275	.0275	NA
	OC	GFDL	.0104	.0122	.0131	.0166
		GISS	.0166	.0135	.0130	
	Nitrate	GISS	.0054	.0057	.0060	
	Total	**GFDL**	**.1715**	**.1964**	**.1660**	**.1411**
		GISS	**.1959**	**.2007**	**.1934**	**NA**
		NCAR	**.116**	**.1392**	**.1206**	**NA**
Northern Hemisphere	BC	GFDL	.0109	.0147	.0161	.0209
		GISS	.0062	.0043	.0032	NA
	Sulfate	GFDL	.1509	.1766	.1038	.0694
		GISS	.0352	.0449	.0388	NA
		NCAR	.078[**]	.097[**]	.073[**]	NA
	Dust	GISS	.0600	.0642	.0615	
		GFDL	.0491	.0491	.0491	.0491
	Sea-salt	GISS	.0630	.0619	.0647	
		GFDL	.0181	.0181	.0181	.0181
	Total	**GFDL**	**.2430**	**.2756**	**.2056**	**.1807**
		GISS	**.1910**	**.1985**	**.1907**	**NA**
		NCAR	**.1538**	**.1827**	**.1502**	**NA**
Southern Hemisphere	BC	GFDL	.0042	.0046	.0049	.0066
		GISS	.0029	.0026	.0023	NA
	Sulfate	GFDL	.0526	.0689	.0774	.0487
		GISS	.0148	.0175	.0170	NA
		NCAR	0.052[**]	.062[**]	.075[**]	
	Dust	GISS	.0144	.0137	.0159	
		GFDL	.0071	.0071	.0071	.0071
	Sea-salt	GISS	.1502	.1541	.1453	
		GFDL	.0291	.0291	.0291	.0291
	Total	**GFDL**	**.1000**	**.1171**	**.1263**	**.1015**
		GISS	**.1997**	**.2030**	**.1962**	**NA**
		NCAR	**.0779**	**.0957**	**.0910**	**NA**

2049   [**] Total for sulfate + sea salt.

2050

2051

2052   **3.3 Climate Studies**

2053   **3.3.1 Experimental Design**

2054   The climate studies discussed here consisted of transient climate simulations that were

2055   designed to isolate the climate effects of projected changes in the short-lived species and

2056   calculate their importance relative to that of the long-lived well-mixed greenhouse gases.

2057   The simulations from the GFDL, GISS, and NCAR groups each employed ensembles

2058   (multiple simulations differing only in their initial conditions) in order to reduce the

2059   unforced variability in the chaotic climate system. One three-member ensemble included

2060   the evolution of short- and long-lived species following the A1B scenario, while the

2061   second ensemble included only the evolution of long-lived species with the short-lived

2062   species fixed at present values. While all three groups used the same values for the long-

2063   lived species, each had its own version of an A1B scenario for short-lived species, as

2064   discussed previously in Section 3.2.

2065

2066   The global three-dimensional distributions of short-lived gases and aerosols were

2067   modeled using each group's chemistry-aerosol composition model. For the first

2068   ensemble, the GFDL simulations used aerosol and ozone distributions computed each

2069   decade out to 2100, while the GISS and NCAR simulations employed values computed

2070   for 2000, 2030, and 2050. Either seasonally varying or monthly-average three-

2071   dimensional distributions were saved. Short-lived species concentrations for intermediate

2072   years were linearly interpolated between the values for computed years. In both sets of

2073   simulations, the concentrations of long-lived species varied with time. In practice, NCAR

2074   performed only a single pair of simulations out to 2050, while GISS performed all three

2075   pairs out to 2050, and GFDL extended all three pairs out to 2100.

2076

2077   **3.3.2 Climate Models**

2078   **3.3.2.1 Geophysical Fluid Dynamics Laboratory (GFDL)**

2079   Climate simulations at GFDL used the comprehensive climate model (Atmosphere-

2080   Ocean General Circulation Model (AOGCM); see Box 1.1) recently developed at

2081   NOAA's Geophysical Fluid Dynamics Laboratory, which has described in detail in

2082   (Delworth *et al.*, 2006). The control simulation of this AOGCM (using present-day

2083   values of radiatively active species) has a stable, realistic climate when integrated over

2084   multiple centuries. The model is able to capture the main features of the global evolution

2085   of observed surface temperature for the 20th century as well as many continental-scale

2086   features (Knutson *et al.*, 2006). Its equilibrium climate sensitivity to a doubling of CO_2 is

2087   3.4°C[37] (Stouffer *et al.*, 2006). The model includes the radiative effects of well-mixed

2088   gases and ozone on the climate as well as the direct effects of aerosols, but does not

2089   include the indirect aerosol effects (see Box 3.1). Further details on the model resolution,

2090   model physics, and model performance are included in Appendix 3.2 (Climate Models) in

2091   the section on Geophysical Fluid Dynamics Laboratory.

2092

2093   **3.3.2.2 Goddard Institute for Space Studies (GISS)**

2094   The GISS climate simulations were performed using GISS ModelE (Schmidt *et al.*,

2095   2006). This model has been extensively evaluated against observations (Schmidt *et al.*,

---

[37] Equilibrium climate sensitivity is defined here as the global -mean annual- mean surface temperature
change of a climate model in response to a doubling of atmospheric carbon dioxide from preindustrial
levels, when the model has fully adjusted to the change in carbon dioxide.

2096   2006), and has a climate sensitivity in accord with values inferred from paleoclimate data

2097   and similar to that of mainstream General Circulation Models.; the equilibrium climate

2098   sensitivity for doubled CO_2 is 2.6°C. The radiatively active species in the model include

2099   well-mixed gases, ozone, and aerosols. The model includes a simple parameterization for

2100   the aerosol indirect effect (Menon *et al.*, 2002) (see box on aerosol indirect effect).

2101   Further details on the model resolution and model physics are included in Appendix 3.2

2102   (Climate Models) in the section on Goddard Institute for Space Studies.

2103

2104   **3.3.2.3 National Center for Atmospheric Research (NCAR)**

2105   The transient climate simulations use the NCAR Community Climate System Model

2106   CCSM3 (Collins *et al.*, 2006). The equilibrium climate sensitivity of this model to

2107   doubled CO_2 is 2.7°C. Further details on the model resolution and construction are found

2108   in Appendix 3.2 (Climate Models) in the section on National Center for Atmospheric

2109   Research.

2110

> **Box 3.1: Radiative Effects of Aerosols**
>
> The direct effects of aerosols refer to their scattering and absorption of both incoming solar and outgoing terrestrial radiation. By reflecting incoming radiation back to space, most aerosols have a negative radiative forcing (cooling effect). For reflective aerosols (sulfate, organic carbon, nitrate, dust and sea-salt), this effect dominates over their absorption of outgoing radiation (the greenhouse effect) on the global scale. The balance varies both geographically and seasonally as a function of solar radiation and the ground temperature. In contrast, absorbing aerosols such as black carbon have a positive radiative forcing (warming effect) as they absorb incoming and outgoing radiation, reducing the overall fraction of the sun's irradiance that it reflected back to space. They can also absorb outgoing radiation from the Earth (the greenhouse effect).
>
> In addition to their direct radiative effects, aerosols may also lead to an indirect radiative forcing of the climate system through their effect on clouds. Two aerosol indirect effects are identified: The first indirect effect (also known as the cloud albedo effect) occurs when an increase in aerosols causes an increase in cloud droplet concentration and a decrease in droplet size for fixed liquid water content (Twomey, 1974). Having more, smaller drops increases the cloud albedo (reflectivity). The second indirect effect (also known as the cloud lifetime effect) occurs when the reduction in cloud droplet size affects the precipitation efficiency, tending to increase the liquid water content, the cloud lifetime (Albrecht, 1989), and the cloud thickness (Pincus and Baker, 1994). As the clouds last longer, this leads to an increase in cloud cover. It has been argued that empirical data suggest that the second indirect effect is the dominant process (Hansen *et al.*, 2005).
>
> The direct effects of aerosols are relatively well-represented in climate models such as those described in Section 3.3.2 and used in this study, though substantial uncertainties exist regarding the optical properties of some aerosol types and especially of aerosol mixtures. Because of the inherent complexity of the aerosol indirect effect, climate model studies dealing with its quantification necessarily include an important level of simplification. While this represents a legitimate approach, it should be clear that the climate model estimates of the aerosol indirect effect are very uncertain.
>
> The studies discussed in chapter 3 of this report include the direct effects of aerosols in all three models (though nitrate is only included in the GISS model). The indirect effect is only included in the GISS model, which uses a highly simplified representation of the second indirect effect.

2111

3.3.3 Radiative Forcing Calculations

2113 The radiative forcing at the tropopause provides a useful, though limited, indicator of the

2114 climate response to perturbations (Hansen *et al.*, 2005) (see Box 3.2).

2115

2116

> **Box 3.2: Radiative Forcing**
>
> **Radiative forcing** is defined as the change in net (down minus up) irradiance (solar plus longwave, in W m^{-2}) at the tropopause due to a perturbation after allowing for stratospheric temperatures to adjust to radiative equilibrium, but with surface and tropospheric temperatures and state held fixed at the unperturbed values (IPCC, 2007; Ramaswamy et al, 2001). This quantity is also sometimes termed adjusted radiative forcing. If the stratospheric temperatures are not allowed to adjust, the irradiance change is termed instantaneous radiative forcing.
>
> The utility of the radiative forcing concept is that, to first order, the equilibrium global-mean, annual-mean surface temperature change is proportional to the radiative forcing, for a wide range of radiative perturbations (WMO, 1986). The proportionality constant (often denoted as the climate sensitivity parameter, λ) is approximately the same (to within 25%) for most drivers of climate change (IPCC, 2007), with a typical value of ~0.5-0.7 for most models . This enables a readily calculable and comparable measure of the climate response to radiative perturbations, such as those discussed in this Chapter.

2117

2118   **3.3.3.1 Global and Hemispheric Average Values: GFDL and GISS**

2119   Radiative forcing calculations were performed by GFDL (adjusted forcing) and GISS

2120   (instantaneous forcing), but were not performed for the NCAR model. The annual-

2121   average global-mean radiative forcing (RF) from short-lived species at 2030 relative to

2122   2000 is small in both the GFDL and GISS models (Figure 3.3; Table 3.6). However, this

2123   is for quite different reasons. In the GFDL model, a large increase in sulfate optical depth

2124   leads to a negative forcing that is largely balanced by positive forcings from increased

2125   black carbon aerosol and ozone. In the GISS model, increased sulfate and reduced black

2126   carbon both lead to relatively small negative forcings that largely offset a substantial

2127   positive forcing from increased ozone. Moving to 2050, the models now diverge in their

2128   net values as well as the individual contributions. The GFDL model finds a positive

2129   radiative forcing due in nearly equal parts to increased black carbon and ozone. In

2130   contrast, 2050 radiative forcing in the GISS model again reflects an offset between

2131   positive forcing from ozone and negative aerosol forcing, with the largest contribution to

2132   the latter from reduced levels of black carbon. Both models show a partial cancellation of

2133   the black carbon forcing by an opposing forcing from organic carbon. Thus, the two

2134   models show somewhat consistent results for ozone, but differ dramatically for black

2135   carbon and sulfate aerosol. By 2100, the GFDL model has a large positive radiative

2136   forcing relative to 2000, due to the continued increase in black carbon as well as the

2137   decrease in sulfate.

2138
2139   **Table 3.6 Global mean radiative forcing for short-lived species (W m^{-2})**

	Model	2030	2050	2100
Total	GFDL	.04	.48	1.17
	GISS	.00	.02	NA
Aerosols	GFDL	-.15	.24	.98
	GISS	-.13	-.17	NA
Sulfate	GFDL	-.32	.01	.51
	GISS	-.10	-.06	NA
BC	GFDL	.21	.30	.63
	GISS	-.09	-.16	NA
OC	GFDL	-.04	-.06	-.15
	GISS	.06	.06	NA
Ozone	GFDL	.19	.23	.19
	GISS	.13	.19	NA

2140   Values are annual average radiative forcings at the tropopause (meteorological tropopause in the GISS
2141   model, 'linear' tropopause in the GFDL model). 'Aerosols' is the total of sulfate, black carbon (BC), and
2142   organic carbon (OC) (plus nitrate for GISS). GISS values do not include aerosol indirect effects that were
2143   present in that model.
2144   GFDL values are for adjusted radiative forcing; GISS values are for instantaneous radiative forcing (see
2145   Box 3.2). The GFDL values are from (Levy *et al.*, 2007).
2146

2147   Inter-model differences in radiative forcing are predominantly due to differences in

2148   modeled burdens rather than to differences in the calculation of radiative properties in the

2149   models. This can be seen clearly by examining the RF-to-burden ratio, which we term the

2150   radiative efficiency (Table 3.7). This shows fairly similar values for GFDL and GISS.

2151   The largest differences are seen for black carbon, which may reflect differences in the

2152   geographic location of projected black carbon changes as well as differing treatments of

2153   the radiative properties of black carbon. Additionally, the vertical distribution of the

2154   black carbon changes will affect the radiative forcing, as will their location relative to

2155   clouds. Variations in modeling the aerosol uptake of water, which can have a substantial

2156   impact on the aerosol optical depth , do not seem to play a very large role in the global

2157   mean radiative forcing judging from the fairly close agreement in the two models' sulfate

2158   radiative efficiencies (Table 3.7). They may contribute to the ~20% difference in the RF-

2159   to-burden ratios for sulfate, however. Examination of the RF-to-aerosol optical depth

2160   change (Table 3.7) shows that given a particular aerosol optical depth change, the models

2161   are in good agreement as to the resulting radiative forcing. We caution that this result

2162   contrasts with a wider model study that found larger differences in this ratio (Schulz *et*

2163   *al.*, 2006), though the variation in RF-to-aerosol optical depth across models was still

2164   less than the variation in aerosol optical depth itself. This suggests a possible further

2165   source of model differences that could exist were different models to be used in a study

2166   such as this.

2167
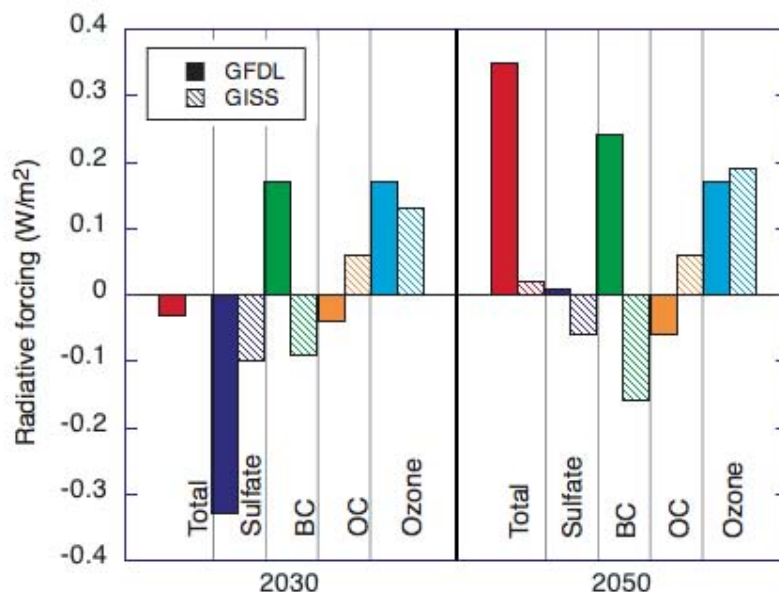
2168
2169 **Figure 3.3** Global mean annual average radiative forcing (in W m^{-2}) from short-lived species at 2030 and
2170 2050 relative to 2000. Values from the GFDL model are shown as solid bars; values from the GISS model
2171 have diagonal hatching. (Note that instantaneous forcing values from the GFDL model are shown in this
2172 figure, not the adjusted forcings shown in Table 3.6.)

2173
2174 Both the GFDL and GISS models show a positive forcing from ozone that stems partially

2175 from increased tropospheric ozone concentrations (Table 3.2) due to increased NO$_x$

2176 emissions (Table 3.1) and partially from the recovery of stratospheric ozone due to

2177 reductions in emissions of ozone-depleting substances (primarily halogens). The forcing

2178 from the tropospheric portion of the ozone changes is substantially more important,

2179 however (Shindell *et al.*, 2007). (The NCAR group did not calculate the radiative forcing,

2180 but forcing in their model is likely to have been similar, as they found an increase in the

2181 tropospheric ozone burden from 2000 to 2050 of 15.0 Dobson Units (DU), very close to

2182 the GISS value of 16.2 DU (Table 3.2).) As shown previously, however, the apparent

2183 sensitivity of ozone burden to changes in NO$_x$ emissions differs substantially between the

2184 GISS and GFDL models. Thus the similarity in the radiative forcing may be largely

2185   fortuitous, resulting from a cancellation of changes in emissions and of sensitivities of

2186   ozone to NO_x emissions.

2187

2188   Thus, at 2030, differences in the physical processes in the two models dominate the

2189   differences in radiative forcing between the two models. The large divergence in

2190   radiative forcing from sulfate stems from both the chemical conversion efficiency of SO_2

2191   to sulfate being more than a factor of two larger in the GFDL model than in the GISS

2192   model, and the greater role of sulfate in producing aerosol optical depth in the GFDL

2193   model. In addition, the GISS model includes a substantial absorption of sulfate onto dust,

2194   a process that is highly uncertain. Such a process would reduce the radiative forcing due

2195   to sulfate. At 2050, emissions and concentrations of sulfur dioxide have returned to near

2196   their 2000 level, so that these differences are not so important at this time. Hence, the

2197   2050 differences between the two models are dominated by differences in black carbon

2198   emissions projections and not by differences in physical processes. Differences in the

2199   residence times and radiative efficiencies for black carbon are substantial but tend to

2200   offset.

2201
2202   **Table 3.7 Radiative efficiency.**

Species	Model	$(W\ m^{-2})/Tg$	$(W\ m^{-2})/AOD$
BC	GFDL	2.8	104
	GISS	1.5	94
OC	GFDL	-0.18	NA
	GISS	-0.16	NA
Sulfate	GFDL	-.47	-16
	GISS	-.59	-16

2203   Values are given for the radiative efficiency in terms of the RF-to-burden ratio and the RF-to-aerosol
2204   optical depth (AOD) ratio. All values are global-mean, annual-mean averages. Values for radiative forcing
2205   and burden or aerosol optical depth changes are for 2050 versus 2000 for black carbon (BC) and organic
2206   carbon (OC), and 2030 versus 2000 for sulfate in order to analyze the largest changes for each species.
2207   GISS values for the sulfate burden changes include only the portion of sulfate not absorbed onto dust, as
2208   this portion alone is radiatively important.

2209

2210   On a hemispheric scale, the GISS and GFDL models again differ greatly (Table 3.8). The

2211   GFDL model shows a very large positive forcing in the Northern Hemisphere in 2050

2212   due primarily to reductions in emissions of sulfate precursors and increased emissions of

2213   black carbon. Increases in sulfate precursor emissions from developing countries lead to a

2214   negative forcing in the Southern Hemisphere in the GFDL model. In the GISS model, the

2215   sign of the total net forcings are reversed, with negative values in the Northern

2216   Hemisphere and positive in the Southern Hemisphere (Table 3.8). The GISS results are

2217   primarily due to the reduction in BC in the Northern Hemisphere and the influence of

2218   increased ozone and reduced OC in the Southern Hemisphere (where sea-salt dominates

2219   the aerosol optical depth, so that anthropogenic aerosol emissions changes are relatively

2220   less important).

2221
2222   **Table 3.8 Hemispheric radiative forcing (W m^{-2}).**

	Model	2030	2050	2100
Northern	GFDL	.15	1.09	1.91
Hemisphere	GISS	-.15	-.14	NA
Southern	GFDL	-.09	-.14	.42
Hemisphere	GISS	.16	.18	NA

2223   Values are the net annual average forcings at the tropopause in each hemisphere from aerosols and ozone.
2224   GISS forcing values do not include aerosol indirect effects that were present in that model.
2225

2226   **3.3.3.2 Regional Forcing Patterns**

2227   The differences in hemispheric and global forcings can be attributed to strong forcing

2228   changes in particular regions, and hence to regional emissions as the radiative forcing is

2229   typically localized relatively close to the region of emissions. Comparison of the spatial

2230   patterns of radiative forcing in the GISS and GFDL models reveals that the starkest

2231   discrepancies occur in the developing nations of South and East Asia (Figure 3.4). The

2232   emissions scenario used by the GISS model projects strong increases in SO_2 emissions

2233   from India, with little change over China. In contrast, the scenario used by the GFDL

2234   model has large decreases in sulfate emissions in both regions, especially China.

2235

2236   The scenarios are much more similar for the developed world, with both projecting

2237   reductions in sulfate precursor emissions for North America and Europe, for example,

2238   leading to a positive radiative forcing in both cases. Differences between the scenarios

2239   are even larger for black carbon, which increases throughout most of the Northern

2240   Hemisphere in the GFDL model but decreases in the GISS model. Again, however, the

2241   divergence is especially large over South and East Asia, where the GISS model has large

2242   reductions while the GFDL model has large increases (Figure 3.4). Thus the differences

2243   in the global total emissions discussed previously (Figure 3.1; Table 3.1) and in the

2244   global radiative forcing (Figure 3.2; Table 3.6) arise primarily from differences in

2245   projected emissions from developing countries in Asia.

2246

2247   The radiative forcing from organic carbon is generally similar in its spatial pattern to

2248   black carbon, but of opposite sign and substantially reduced magnitude (25-40% of the

2249   black carbon radiative forcing). Substantial differences again occur between the

2250   emissions scenarios of the two models, this time primarily over African biomass burning

2251   regions. As discussed previously, the GFDL model assumed that biomass burning

2252   emissions would scale with ½ the factor used for purely anthropogenic emissions, while

2253   the GISS model instead used regional biomass burning emissions projections from

2254   (Streets *et al.*, 2004), with substantial reductions in African biomass burning.

2255

2256   The spatial pattern of radiative forcing from ozone is also very different in the two

2257   models (Figure 3.4). However, this forcing is not so closely tied to the region of precursor

2258   emissions in the GISS model where much of the forcing is related to an increased flux of

2259   ozone into the troposphere owing to the recovery of lower stratospheric ozone. This leads

2260   to substantial positive forcing in that model at high latitudes, even without including the

2261   effects of climate change on circulation (see section 3.3.3.4). At low latitudes, GISS

2262   shows little forcing as the modeled increase in upper stratospheric ozone causes cooling

2263   which offsets part of the warming caused by lower stratospheric ozone increases.

2264   Additionally, the overall increase in overhead stratospheric ozone reduces the

2265   photochemical formation of ozone in the troposphere, offsetting some of the

2266   enhancement there due to increased precursor emissions. The GFDL model does not

2267   show a similar high latitude enhancement, however, but instead shows maximum ozone

2268   forcing in the tropics. This may reflect a greater geographic shift in emissions to lower

2269   latitudes, a greater efficiency in transporting ozone and its precursors to the upper

2270   troposphere, where ozone has the greatest positive forcing efficiency, and differences in

2271   the relative importance of change in the overlying stratospheric ozone column. The

2272   GFDL radiative forcing is similar to results from models with tropospheric ozone only

2273   (Gauss *et al.*, 2003).

2274
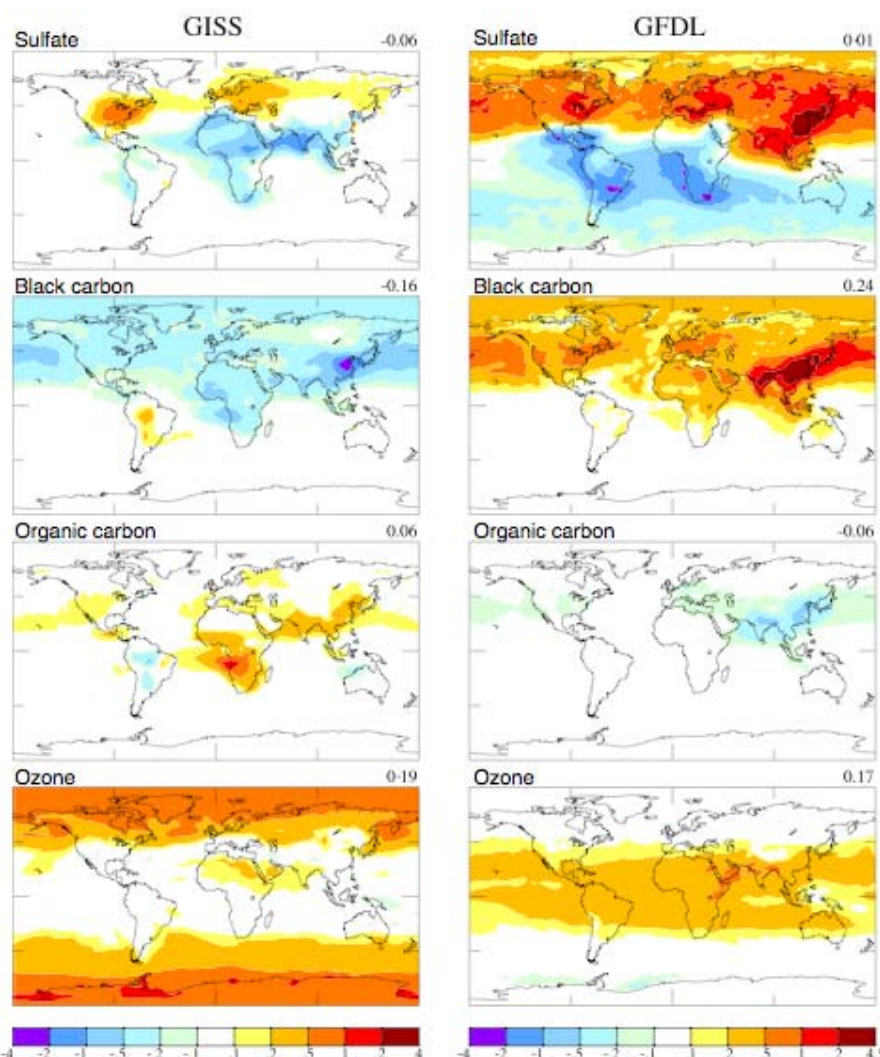
2275
Figure 3.4 Annual average instantaneous radiative forcing (W m^{-2}) near 2050 relative to 2000 for the indicated individual short-lived species in the GISS (left) and GFDL (right) models. Radiative forcing from long-lived species is largely spatially uniform over the globe. (Note that the instantaneous forcings shown here for the GFDL model differ from the adjusted forcings show in Table 3.6.).

3.3.3.3 Effects of uncertainties in methane concentrations on radiative forcing

The SAP 3.2 simulations included methane concentrations prescribed to A1B values from

the AIM integrated assessment model, for consistency with the long-lived species runs.

To investigate the potential uncertainty in the methane value derived by that integrated

assessment model , the GISS model performed an additional 2050 simulation using its

2286   internal methane cycle model (Shindell *et al.*, 2007). The simulation included prescribed

2287   anthropogenic emissions increases from the AIM model to allow comparisons with the

2288   AIM results used in the results in this report (SAP 3.2). Natural spatially and seasonally

2289   varying emissions and soil adsorption were the standard amounts described in (Shindell

2290   *et al.*, 2003). Both the methane emissions from wetlands and the biogenic isoprene

2291   emissions were interactive with the climate in this run (Guenther *et al.*, 1995; Shindell *et*

2292   *al.*, 2004), though the distribution of vegetation did not respond to climate change.

2293

2294   Methane's oxidation rate is calculated by the model's chemistry scheme in both the

2295   troposphere and stratosphere. Thus methane can affect its own lifetime (which is

2296   primarily governed by tropospheric oxidation rates), as can other molecules that compete

2297   with methane for hydroxyl radicals (the main oxidizing agent), such as isoprene. The

2298   simulations included 2050 surface climate (sea-surface temperatures and sea ice, taken

2299   from an earlier climate model run). Changes in water vapor induced by the altered

2300   climate affect methane oxidation in those runs. Methane was initialized with estimated

2301   2050 abundances and the simulations were run for 3 years. We note that the IMAGE

2302   integrated assessment model projected a continuous increase in methane emissions, rather

2303   different from the increase through 2030 and slow decrease thereafter in the AIM

2304   integrated assessment model. At 2050, for example, this led to projected anthropogenic

2305   methane emissions of 512 Tg/yr in the IMAGE model, substantially greater than the 452

2306   Tg/yr from the AIM model used here (compared with 323 Tg/yr for 2000).

2307

2308   We find that methane emissions from wetlands increase from 195 to 241 Tg/yr while

2309   emissions of isoprene increase from 356 to 555 Tg/yr. Additionally, even in the absence

2310   of changes in emissions from natural sources, the projected anthropogenic emissions of

2311   ozone precursors (including methane itself) increase the lifetime of methane while

2312   climate change reduces it via increased temperature and water vapor (Table 3.9). These

2313   responses to anthropogenic emissions and to climate change without interactive

2314   emissions are qualitatively consistent with those reported from a range of models (using

2315   different emissions projections) in (Stevenson *et al.*, 2006). The effect of precursor

2316   emissions is stronger in our scenario, so that the net effect of anthropogenic emissions

2317   and climate changes is to increase methane's lifetime. When natural emissions are also

2318   allowed to respond to climate change, increased competition from isoprene and increased

2319   methane emissions from wetlands lead to further increases in methane's lifetime (Table

2320   3.9) and enhanced methane abundance.

2321

2322   The 2050 simulation with the model's internal methane cycle had a global mean surface

2323   methane value of 2.86 ppmv in year 3, with sources exceeding sinks by 80 Tg/yr (a

2324   growth rate that may reflect an overestimate of the loss rate in the AIM model used in the

2325   initial guess). Extrapolating the change in methane out to equilibrium using an

2326   exponential fit to the three years of model results yields a 2050 value of 3.21 ppmv.

2327

2328   We have calculated radiative forcings using the standard calculation (Table 6.2 in

2329   (Ramaswamy *et al.*, 2001)) assuming an increase in N_2O from 316 to 350 ppb in 2050,

2330   following the A1B 'marker' scenario (using the AIM integrated assessment model). The

2331   2050 methane forcing using the methane concentration specified in the A1B 'marker'

2332   scenario would be 0.22 W m^{-2} while using the larger methane concentrations of 2.86 or

2333   3.21 ppmv calculated with our model gives 0.36 or 0.46 W m^{-2}, respectively. Of course, it

2334   is difficult to estimate methane's abundance at a particular time without performing a full

2335   transient methane simulation. However, uncertainty in the forcing from methane appears

2336   to be at least 0.1-0.2 W m^{-2}. Note that use of the 40% larger anthropogenic methane

2337   emission increase from the IMAGE integrated assessment model would have led to a

2338   substantially larger forcing. Should the results of our modeling of the methane cycle

2339   prove to be fairly robust, this would imply that future positive forcing from methane

2340   might be substantially larger than current estimates based on integrated assessment model

2341   projections.

2342

2343   We note that while the A1B projections assume a substantial increase in atmospheric

2344   methane in the future, the growth rate of methane has in fact decreased markedly since

2345   the early 1990s and leveled off since ~1999 (Dlugokencky *et al.*, 2003). Hence, the

2346   projections may overestimate future atmospheric concentrations. However, there are

2347   indications that the growth rate decrease was primarily due to reduced anthropogenic

2348   emissions, and that these have been increasing again since 1999 (though masked by a

2349   coincident decrease in natural methane emissions) (Bousquet *et al.*, 2006). All of this

2350   suggests that atmospheric methane may in fact increase substantially again in the future,

2351   as assumed by the integrated assessment models, although other methane studies have

2352   argued for an increase in its principle loss path as the explanation, rather than changes in

2353   emissions (*e.g.* Fiore *et al.*, 2006). Other emissions, such as NOx from lightning and from

2354   soil and dimethyl-sulfide from the oceans, are also expected to respond to climate

2355   change. Changes in land cover would also affect both emissions and removal of trace

2356   species. Further work is required to gauge the importance of these and other climate-

2357   chemistry feedbacks.

2358   **Table 3.9** Methane lifetime in GISS simulations. Includes calculated photochemical loss (in troposphere
2359   and stratosphere) and prescribed 30 Tg/yr loss to soils.

Run	Lifetime (years)
2000	9.01
2030	9.96
2050	10.39
2030 with climate change	9.72
2050 with climate change	10.01
2050 with methane cycle	10.42

2360

2361   **3.3.3.4 Effects of Climate Change on Radiative Forcing**

2362   The chemical composition simulations (Section 3.2) did not include the effects of climate

2363   change on the short-lived species, only the effects of projected changes in anthropogenic

2364   emissions. Separate sets of simulations with the GISS model included climate change via

2365   prescribed sea-surface temperatures and sea-ice cover taken from prior runs. Climate

2366   change increased the radiative forcing from ozone by increasing stratosphere-troposphere

2367   exchange (STE) and hence ozone near the tropopause where it is most important

2368   radiatively (Hansen *et al.*, 1997). This effect outweighed increased reaction of excited

2369   atomic oxygen with the enhanced tropospheric water vapor found in a warmer climate,

2370   which led to ozone reductions in the tropical lower troposphere. The overall impact was

2371   to increase radiative forcing by .07 W m^{-2} in 2050. Climate change slightly increased the

2372   negative forcing from sulfate (by .01 W m^{-2}), consistent with an increase in tropospheric

2373   ozone in these runs (as ozone aids in sulfur dioxide oxidation both directly and via

2374   hydroxyl formation).

2375

2376   Dust emissions decreased slightly (~5% at 2050) in these climate runs, but there was

2377   more sulfate on dust, suggesting that this played only a minor role in the sulfate forcing

2378   response to climate change. The reduction in dust would itself lead to a slight negative

2379   forcing (~0.02 W m^{-2}). However, emissions in the model respond only to changes in

2380   surface wind speeds, and not to changes in sources due to either CO_2 fertilization or

2381   climate-induced vegetation changes which have a very uncertain effect on future dust

2382   emissions (Mahowald and Luo, 2003; Woodward *et al.*, 2005).

2383

2384   Much of the increase in ozone forcing results from an increase in stratosphere-

2385   troposphere exchange in the GISS model of 134 Tg/yr (~27% of its present-day value) as

2386   climate warms. An increase in transport rates between the stratosphere and the

2387   troposphere is a robust projection of climate models (Butchart *et al.*, 2006). Combined

2388   with the expected recovery of stratospheric ozone, this should enhance the influx of

2389   stratospheric ozone into the lower atmosphere. However, the net effect of climate change

2390   on ozone is more difficult to determine as it results from the difference between enhanced

2391   stratosphere-troposphere exchange and enhanced chemical loss in the troposphere in a

2392   more humid environment, which is not consistent among climate models (Stevenson *et*

2393   *al.*, 2006).

2394

2395   **3.3.4 Climate Model Simulations 2000 – 2050**

2396   As discussed in Section 3.3.1, the experimental design consists of two sets of simulations:

2397   1) the effects of changes in short-lived and long-lived species in the 21st century

2398   (employing the A1B scenario for the evolution of the long-lived species and the output

2399   from the composition models discussed on Section 3.2 for the short-lived species); 2) the

2400   effects of changes in the long-lived species only, with the short-lived species

2401   concentrations held at 2000 values. The effects of short-lived species changes are

2402   determined by subtracting the climate responses of the runs with changes in long-lived

2403   species only from those with changes in long-lived and short-lived species. Simulations

2404   where only the short-lived species change were not included in the experimental design,

2405   because such a scenarios are neither realistic nor policy relevant

2406

2407   **3.3.4.1 Surface Temperature Changes**

2408   The global-mean annual-mean surface temperature responses to short-lived species are

2409   not as dissimilar as one might have expected, given the different emissions used and the

2410   different physical processes included. The NCAR model ran only a single simulation,

2411   which showed little or no statistically significant[38] effects of the short-lived species on

2412   global mean surface temperatures. The GFDL and GISS models both ran 3-member

2413   ensemble simulations, and both show a statistically significant warming effect from

2414   short-lived species from around 2030 to the end of the runs (Figure 3.5). The GFDL

2415   model shows a warming of 0.28 K (ensemble mean 2046-2050). This value is

2416   commensurate with the adjusted radiative forcing of ~0.48 W m^{-2}. computed for 2050.

2417   The GISS model shows substantially more warming, ~0.13 K near 2050, than would be

2418   expected from the direct radiative forcing in that model and its climate sensitivity (λ =

2419   ~0.6 K (W m^{-2})$^{-1}$) owing to the presence of the aerosol indirect effect, which contributes

2420   additional warming as aerosol loading decreases in the future (Shindell *et al.*, 2007).

---

[38] The statistical methods used to assess significance are discussed in Box 3.3.

2421
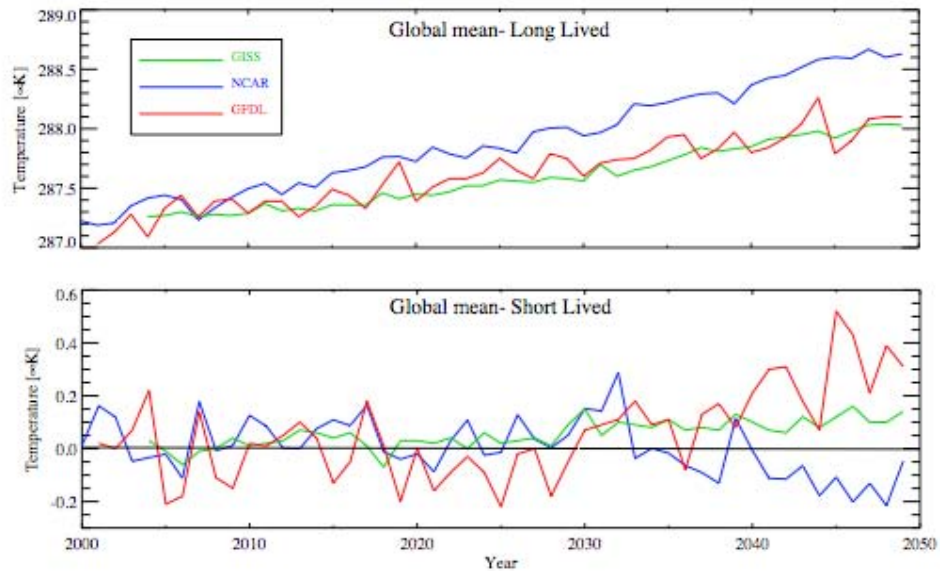
2422
2423 **Figure 3.5** Global mean annual average temperature in the simulations with time-varying long-lived (top)
2424 and short-lived (bottom) species. Results are 3-member ensemble means for GFDL and GISS and single-
2425 member simulations for NCAR. Results for the short-lived species are obtained by subtraction of the (long-
2426 lived) species calculations from the (short + long-lived) species calculations.
2427

2428 The overall global annual average influence of short-lived species is to augment the

2429 warming from well-mixed greenhouse gases by ~20-25% in these two models (17% for

2430 GISS and 27% for GFDL based on 2046-2050 vs. the first 5 years of the run). It is

2431 important to note, however, that these models responded as they did for different reasons.

Box 3.3: Statistical Methods

A result is deemed to be statistically significant if it is unlikely to have occurred by chance (*i.e.*, the probably that it occurred by chance is less than some specified threshold). A 95% confidence level means that the odds are 20:1 against the result having occurred by chance..

Statistical significance in the GFDL climate model results was evaluated using two approaches. For global-mean, or hemispheric-mean results involving a temperature departure from the initial (2000) value, the range (highest to lowest temperature change) of the three ensemble members used to obtain the ensemble-mean result was computed. The ensemble-mean result was deemed significant if that range was entirely different from zero. For regional (latitude-longitude) results comprising the difference of two time series, as in the evolution of temperature change due to short-lived species, the student-t test for significance was applied at each model grid point, with the result deemed significant if the statistical test showed significance at the 95% confidence level.

2432

2433   In the GFDL simulations, reduced sulfate and increased black carbon and ozone all

2434   combined to cause warming. In contrast, in the GISS model, the warming resulted from

2435   increased ozone and a reduced aerosol indirect effect, with a substantial offset (cooling)

2436   from reduced black carbon. The lack of a substantial effect from short-lived species in the

2437   NCAR simulations is attributable to the emissions used, which produced small increases

2438   in sulfate (cooling) and small increases in black carbon (warming) that largely offset one

2439   another (thus their aerosol optical depth changed little from 2000 to 2050).

2440

2441   Hemispheric temperatures show trends largely consistent with the radiative forcings

2442   (Table 3.8), namely substantial warming in the Northern Hemisphere in the GFDL model

2443   and in the Southern Hemisphere in the GISS model (Figure 3.6). The Northern

2444   Hemisphere warming in the GFDL model is driven primarily by the large decreases

2445   projected for sulfate and the large increase projected for black carbon in that model for

2446   the industrialized areas of the Northern Hemisphere (Levy *et al.*, 2007). This causes the

2447   aerosol optical depth from sulfate to drop by 1/3 in the Northern Hemisphere by 2050

2448   while the aerosol optical depth from black carbon increases by 50%. The large change in

2449   sulfate dominates the overall aerosol optical depth change in that model (Table 3.5). The

2450   magnitude of the Northern Hemisphere warming is ~0.5 K by 2050, consistent with the

2451   ~1.1 W m^{-2} radiative forcing in that model, when one accounts for the fact that the

2452   warming has not been fully realized due to the lag-time for oceanic heat adjustment.

2453   There is an overall negative forcing in the Southern Hemisphere in the GFDL model, as

2454   sulfate precursor emissions increase in the developing world while black carbon changes

2455   little. Some of the negative forcing from aerosols in the Southern Hemisphere is offset by

2456   positive forcing from ozone, which increases rather uniformly over much of the world in

2457   that model (Levy *et al.*, 2007), leading to a small net effect and minimal temperature

2458   change from short-lived species (Figure 3.6).

2459

2460   The change in the forcing due to the aerosol indirect effect in the GISS model was argued

2461   to be on the order of 0.1 W m^{-2} in 2050 (Shindell *et al.*, 2007). Combining this with the

2462   GISS hemispheric radiative forcings (excluding the indirect effect) in Table 3.8 yields a

2463   Northern Hemisphere radiative forcing near zero and a Southern Hemisphere forcing of

2464   ~0.3 W m^{-2}. These forcings are consistent with the warming of ~0.15 K seen in that

2465   model in the Southern Hemisphere and the lack of response in the Northern Hemisphere.

2466   Northern Hemisphere aerosol optical depth changes are dominated by a substantial

2467   reduction in black and organic carbon (the black carbon aerosol optical depth in the

2468   Northern Hemisphere falls by nearly 50%), which more than offsets a slight increase in

2469   sulfate (particularly as this model is less sensitive to sulfate). These aerosol changes lead

2470   to negative Northern Hemisphere forcing. In the Southern Hemisphere, the GISS model

2471   shows only small changes in aerosols, so that positive forcing from ozone dominates the

2472   net radiative forcing. The aerosol indirect effect further accentuates the positive forcing

2473   owing to reductions in black carbon and organic carbon. The signs of the temperature

2474   response in the two hemispheres are thus opposite in the GISS model to what they are in

2475   the GFDL model.

2476

2477   As for the global case, trends in the NCAR model are not significantly different in the

2478   runs with and without short-lived species. This is the result of only a miniscule change in

2479   aerosol optical depth in the Northern Hemisphere (-2%), as sulfate and carbonaceous

2480   aerosol precursor emissions are both near their present-day values by 2050 in that model.

2481   In the Southern Hemisphere, there is an increase in aerosol optical depth from 2000 to

2482   2050, which seems to be primarily due to sulfate, but this is largely offset by increased

2483   ozone in the Southern Hemisphere as stratospheric ozone recovers.

2484

2485   Thus it is clear that at global and especially at hemispheric scales, the three climate

2486   models are being driven by substantially different trends in their aerosol species. These

2487   differences in aerosols are largely related to the differences in the projected emissions of

2488   aerosol precursors, though there is some contribution from differences in aerosol

2489   modeling as discussed previously. Additionally, the climate response of each model is

2490   different to some extent owing to the inclusion of different physical processes in the

2491   models, especially the inclusion of the aerosol indirect effect in the GISS model.

2492   However, the above analysis strongly suggests that the largest contributor to the inter-

2493   model variations in projected warming arise from different assumptions about emissions

2494   trends.

2495

2496   At smaller spatial scales, the annual average patterns of surface temperature changes

2497   induced by the short-lived species show even larger divergences (Figure 3.7). Around

2498   2030, the largest responses are seen at Northern middle and high latitudes. These show

2499   large regions of both cooling and warming that are characteristic of the response to

2500   dynamic variations. Surprisingly, all three models show cooling near Alaska and a region

2501   of warming over Siberia. However, most of the response at these latitudes is not

2502   statistically significant in the models owing to large natural variability. Other regions,

2503   such as the Labrador Sea/Baffin Island area or Scandinavia, show substantial variations

2504   between models, again suggesting these middle and high latitude dynamic responses are

2505   not robust.

2506

2507   In the tropics, where dynamic variability is much smaller, the models find much greater

2508   areas with statistically significant responses, especially by 2050. The NCAR model finds

2509   a small but significant cooling over tropical oceans, while the other models find warming.

2510   As in the global-mean case, this appears to arise from differences in aerosol burdens and

2511   optical depths.

2512
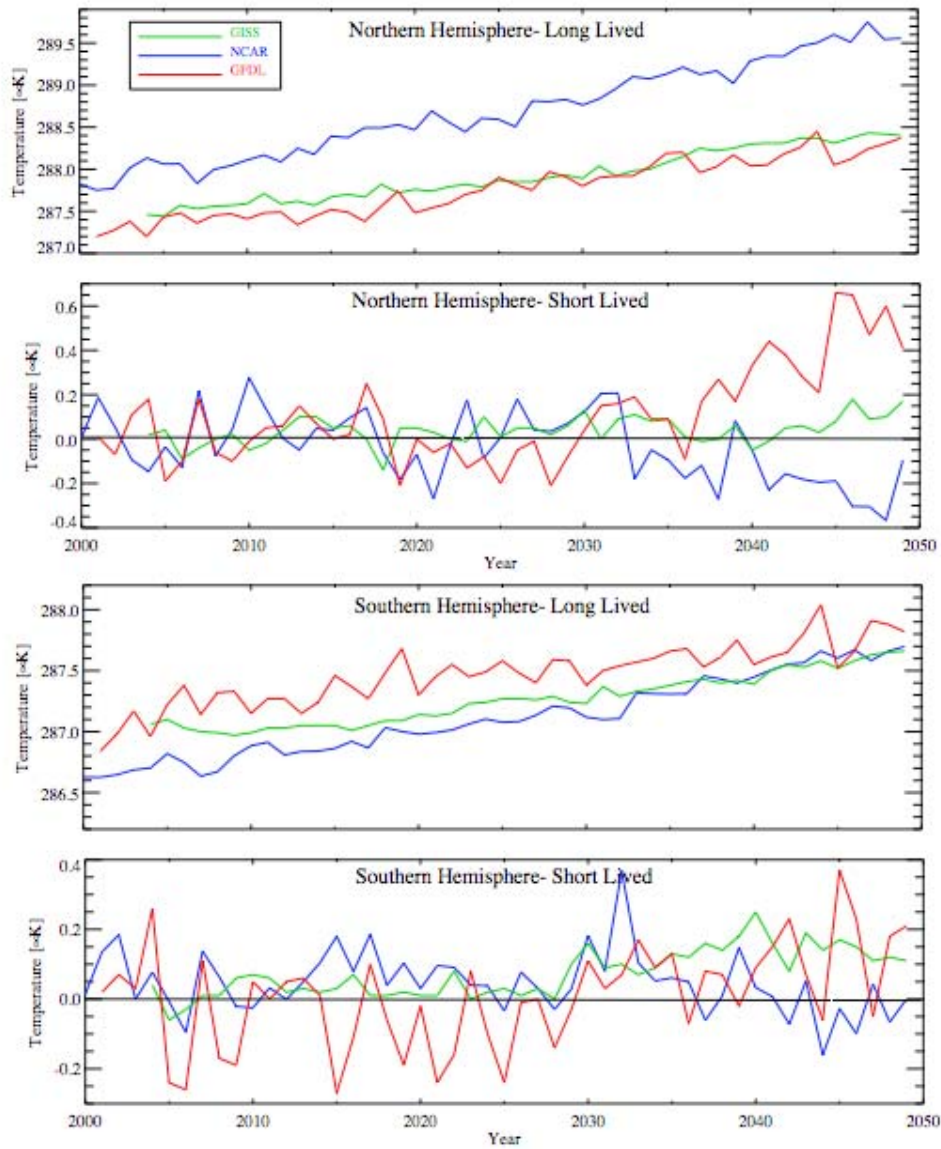
2513
2514   **Figure 3.6** Hemispheric mean annual average temperature in the simulations with time-varying long-lived
2515   and short-lived species. Results are ensemble means for GFDL and GISS.
2516
2517
2518
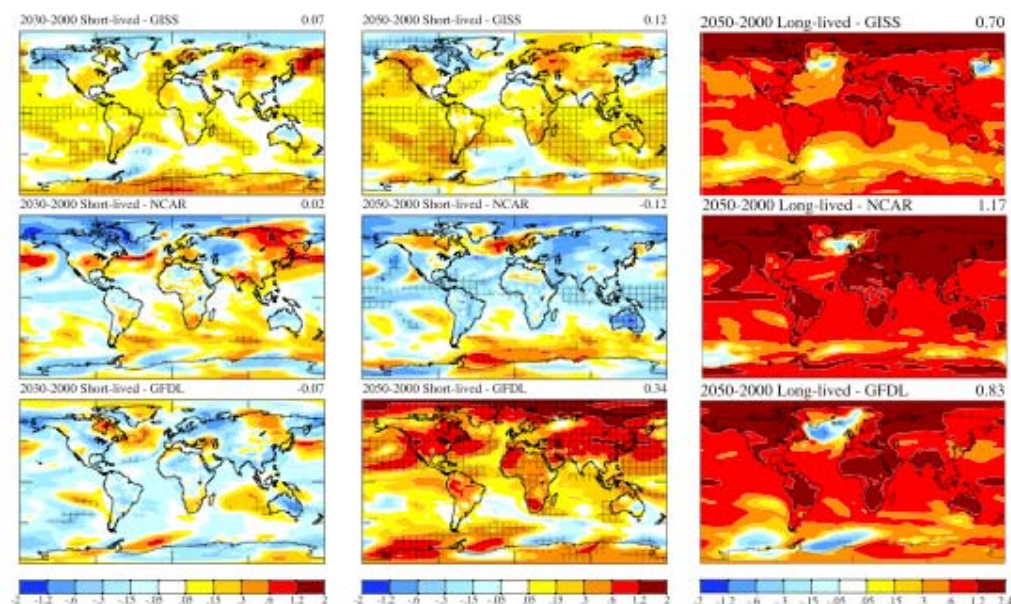
2519
2520 **Figure 3.7** Annual average surface temperature response (K) in the climate models to short-lived species
2521 (left and center columns) and long-lived species (right column) changes for the indicated times. The
2522 changes at 2030 are 2020-2029 in the NCAR and GFDL models and 2028-2033 in the GISS model. At
2523 2050, they are 2040-2049 in the NCAR model, 2046-2055 in the GFDL model, and 2040-2050 in the GISS
2524 model. Hatching indicates statistical significance (95%) for the response to short-lived species. Virtually all
2525 colored values are statistically significant in the response to long-lived species. Values in the upper right
2526 corners give the global mean.
2527

2528 In the Arctic, the GISS and NCAR models find primarily a cooling effect from projected

2529 changes in short-lived species (especially near 2030 for GISS, and 2050 for NCAR). In

2530 contrast, the GFDL model finds a substantial warming there. This may be due in part to

2531 the increasing trend in black carbon in that model.

2532

2533 In the Antarctic, the GISS model shows warming related primarily to stratospheric ozone

2534 recovery. The GFDL model shows a similar result by 2050 (after which stratospheric

2535 ozone was unchanged in that model). NCAR does not show as clear an Antarctic

2536 warming, however, even though this model also included recovery of ozone in the

2537 Antarctic lower stratosphere. This is surprising given that the NCAR model appeared to

2538   show a substantial response to ozone depletion in analyses of the Southern Hemisphere

2539   circulation in IPCC AR4 simulations (Miller *et al.*, 2006b). That analysis showed that

2540   most climate models found a general strengthening of the westerly flow in the Southern

2541   Hemisphere in response to stratospheric ozone depletion. A stronger flow isolates the

2542   polar region from lower latitude air, leading to cooling over the Antarctic interior and

2543   warming at the peninsula. Conversely, recovery should lead to warming of the interior

2544   (enhanced by the direct positive radiative forcing from increased ozone), as in the GISS

2545   and GFDL simulations. However, in the GISS model the effect diminishes with time,

2546   suggesting that other aspects of the response to short-lived species become more

2547   important in these scenarios over time, presumably as projected aerosol changes grow

2548   ever larger.

2549

2550   Warming over the central United States is present in the GISS model at all times (but is

2551   not statistically significant), in the GFDL model from about the 2040s on, and in the

2552   NCAR model around 2030, but not at 2050. The United States and other Northern

2553   Hemisphere industrialized regions might be especially sensitive due to the projected

2554   reduction in sulfate precursor emissions in the Northern Hemisphere. This effect is

2555   especially large in the GFDL model, where forcings from sulfate decreases and black

2556   carbon increases both contribute to warming, though it should be noted that the largest

2557   radiative forcing is over Asia, not over the US and Europe (Fig. 3.4). In the NCAR

2558   model, the warming effect vanishes by 2050 as both sulfate and black carbon decrease,

2559   producing temperature responses of opposite sign. In the GISS model, reductions in

2560   sulfate and increases in ozone both contribute to warming; however, these are partially

2561   offset by cooling from reduced black carbon.

2562

2563   The surface temperature changes induced by the long-lived species are clearly much

2564   larger than those induced by short-lived species over most of the Earth by 2050 (Figure

2565   3.7). In some regions, however, the two are of comparable magnitude (*e.g.* the polar

2566   regions and parts of the Northern mid-latitude continents in the GFDL model, parts of the

2567   Southern Ocean in the GISS model). Consistency between the models is also clearly

2568   greater in their response to long-lived than to short-lived species.

2569

2570   Overall, it is clear that the regional surface temperature response does not closely follow

2571   the regional radiative forcing patterns based on either GISS or GFDL results. Both

2572   models show very large forcings over East Asia, for example, yet have minimal response

2573   there. This is especially clear when comparing the seasonal radiative forcings and climate

2574   response (Figure 3.8). Though some of the spatial mismatches could result from a lag in

2575   the climate response to seasonally varying forcings, the divergence between the patterns

2576   of forcing and response is large even for areas with minimal seasonality in the forcing

2577   (*e.g.* Africa, subtropical Asia).

2578
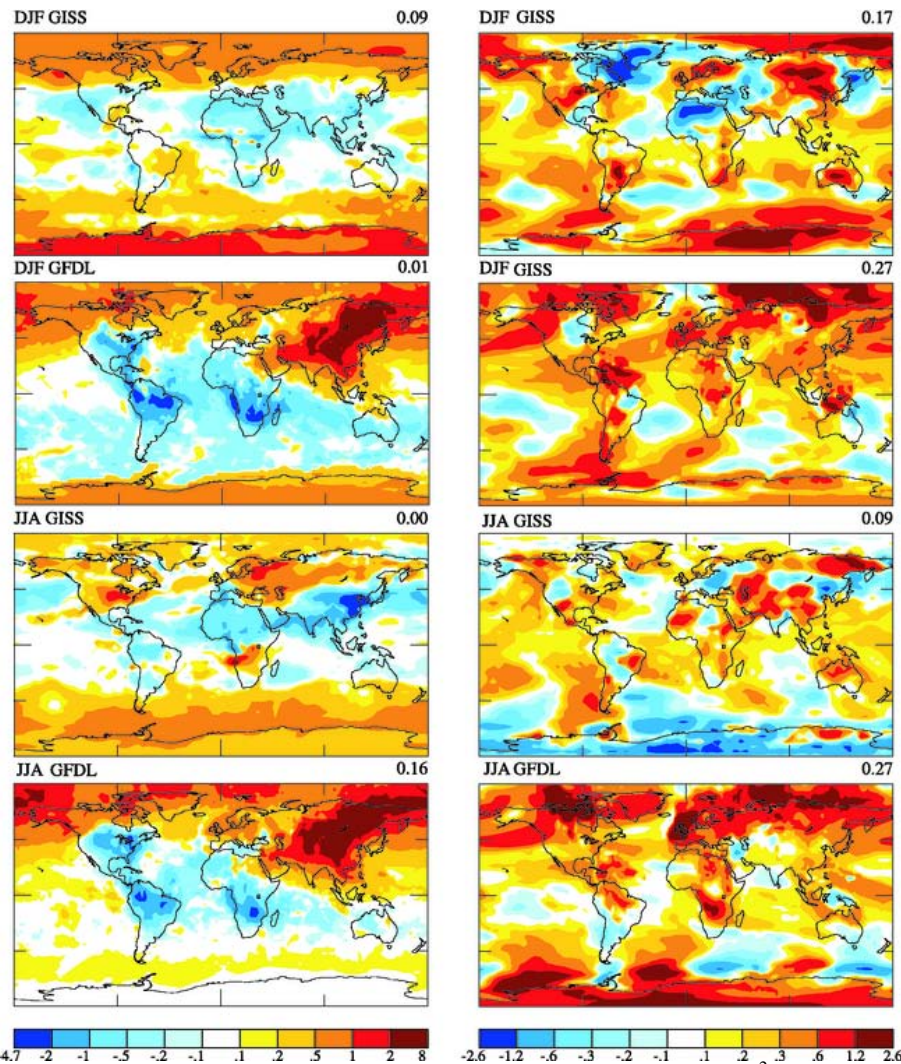
2579
2580 **Figure 3.8** Seasonal average net tropopause instantaneous radiative forcing (W m^{-2}) in 2050 versus 2000
2581 from short-lived species (left column) and surface temperature (K) response (right column) in the GISS and
2582 GFDL models. Boreal winter (December-February) is shown in the top two rows, while boreal summer
2583 (June-August) is shown in the bottom two rows. The temperature changes at 2050 are 2046-2055 in the
2584 GFDL model and 2041-2050 in the GISS model. Values in the upper right corners give the global mean.
2585 (Note that the instantaneous forcings shown here for the GFDL model differ from the adjusted forcings
2586 show in Table 3.6.).
2587

2588 **3.3.4.2 Precipitation, Sea-level Rise, Soil Moisture, etc.**

2589 Changes in other climate parameters such as precipitation or sea level due to short-lived

2590 species are typically too small to isolate statistically. These would generally be expected

2591 to follow the global mean surface temperature change, however, for many of the most

2592 important features. For example, the portion of sea-level rise attributable to thermal

2593   expansion of the oceans would be enhanced by ~20-25% due to short-lived species in the

2594   GISS and GFDL models. Similarly, the enhancement of precipitation along the equator

2595   and drying of the subtropics that is a robust feature of climate models under a warming

2596   climate (Held and Soden, 2006) would also be accentuated under the GFDL and GISS

2597   models with their significant tropical warming, though probably not under the NCAR

2598   scenario. Such a feature can indeed be seen in the GISS response in the Atlantic and

2599   Indian Oceans.

2600

2601   On a regional scale, there are some suggestions of trends but statistical significance is

2602   marginal for either annual or seasonal changes. The NCAR model shows reductions in

2603   winter precipitation due to short-lived species across most of the United States in the

2604   2040s, and reductions in summer precipitation in the southeastern part of the United

2605   States. That model also suggests an increase in summer monsoon rainfall over South

2606   Asia. In contrast, the GISS model shows slight increases in winter precipitation over the

2607   central United States, and a mixed signal in summer (and spring) with increased

2608   precipitation over the Southeast and Southwest United States but decreases over the

2609   Northeast United States. During fall, precipitation decreases over most of the country. As

2610   in the NCAR model, there is an increase in summer (and fall) precipitation over South

2611   Asia. In the annual average, the GFDL model shows no statistically significant trend over

2612   the United States. Given that significant trends are hard to identify in any of the models,

2613   and that the models do not agree on the trends themselves, we believe that it is not

2614   possible to reliably estimate precipitation trends owing to short-lived species changes

2615   under the A1B storyline.

2616

2617   **3.3.4.3 Discussion**

2618   In the transient climate simulations, three climate models examined the response to

2619   projected changes in short-lived species. The results differed substantially among the

2620   models. Comparison has shown that the differences in the underlying emissions

2621   projections, due to differences between the various Integrated Assessment Models that

2622   provided those projections and to assumptions made about emissions not provided by the

2623   Integrated Assessment Models, were the dominant source of inter-model differences in

2624   projected aerosol trends. These were not the only source of differences, however. For

2625   example, the GFDL model's aerosol optical depth is substantially more sensitive to

2626   sulfate than the GISS model, with the NCAR model in between. This is partially due to

2627   the inclusion of sulfate absorption onto dust being present only in the GISS model.

2628   Additionally, the indirect effect of aerosols was included only in the GISS model. Thus,

2629   the inclusion of different physical processes played a role in the inter-model differences,

2630   and was especially important near 2030, when sulfur dioxide (SO_2) emissions were near

2631   their peak. With the inclusion of the aerosol indirect effect, the GFDL model might yield

2632   a substantially larger warming, given that sulfate is the largest contributor to aerosol mass

2633   globally and that the GFDL sulfate concentrations decreased beyond 2030.

2634

2635   Differences were also created by the models' differing simulations of the hydrologic

2636   cycle, which removes soluble species, and oxidation. Inter-model differences between the

2637   GFDL and GISS models in the residence times of aerosols were substantial for sulfate,

2638   and differences in the radiative effect of black carbon were also potentially sizeable. In

2639   nearly all cases, however, these were outweighed by emissions differences. This was not

2640   the case for sulfate at 2030, nor for tropospheric ozone; differences in the modeled

2641   conversion of SO_2 to sulfate and the sensitivity of ozone to NO_x emissions were larger

2642   than differences in projected precursor emissions. Hence, in these cases uncertainties in

2643   physical processes, including chemistry, dominate over uncertainties in emissions.

2644

2645   We also reiterate that uncertainties in the aerosol indirect effect and in internal mixing

2646   between aerosol types are either not included at all or only partially in these simulations.

2647   Sensitivity studies and analysis of the GISS model results indicates that the forcing from

2648   reductions in the aerosol indirect effect was roughly 0.1-0.2 W m^{-2}, while the inclusion of

2649   sulfate absorption onto dust reduced the negative forcing from sulfate at 2030 or 2050 by

2650   up to 0.2 W m^{-2} (Shindell *et al.*, 2007), These sensitivities suggest that uncertainties in

2651   these processes could alter the global mean projected temperature trends by up to 0.1 K at

2652   2030 or 2050, a value comparable to the total temperature trend in that model. Hence

2653   without the aerosol indirect effect, the GISS model would likely have shown minimal

2654   warming, while without sulfate absorption onto dust surface it would like have shown a

2655   substantially greater warming trend (at least at 2030).

2656

2657   The responses of methane (and other hydrocarbon) emissions and of stratosphere-

2658   troposphere exchange to climate change can also potentially have significant impacts on

2659   radiative forcing, and these processes were not included in these simulations. As

2660   discussed in sections 3.3.3.3 and 3.3.3.4, the resulting changes to radiative forcing could

2661   again substantially alter the projected temperature trends. Additionally, given the large

2662   influence of uncertainties in emissions projections, we stress that the magnitude and even

2663   the sign of the effects of short-lived species on climate might be different were alternative

2664   emissions projections used in these same models. Thus, the response of short-lived

2665   species and methane has been only partially characterized by the present study, and

2666   substantial work remains to reduce uncertainties and further clarify the potential role of

2667   short-lived species in future climate change.

2668

2669   The results clearly indicate that the spatial distribution of radiative forcing is generally

2670   less important than the spatial distribution of climate sensitivity in predicting climate

2671   impact. Thus, both short-lived and long-lived species appear to cause enhanced climate

2672   responses in the same regions of high sensitivity rather than short-lived species having an

2673   enhanced effect primarily in or near polluted areas. This result is supported by analysis of

2674   the response to larger radiative perturbations in these models for the future (Levy *et al.*,

2675   2007) and the past (Shindell *et al.*, 2007). It is also consistent with earlier modeling

2676   studies examining the response to different inhomogeneous forcings than those

2677   investigated here (Mitchell *et al.*, 1995; Boer and Yu, 2003; Berntsen *et al.*, 2005;

2678   Hansen *et al.*, 2005).This suggests that the mismatch between model simulations of the

2679   regional patterns of 20th century climate trends and observations is likely not attributable

2680   to unrealistic spatially inhomogeneous forcings imposed in those models. Instead, the

2681   models may exhibit regional climate sensitivities that do not match the real world, and/or

2682   some of the observed regional changes may have been unforced.

2683

2684

**3.3.5 Climate Simulations Extended to 2100**

2685

2686   Following the A1B "marker" scenario into the second half of the 21st century for both

2687   three-member ensembles, the GFDL simulations (Levy *et al.*, 2007) find significant

2688   climate impacts due to emissions of sulfur dioxide (SO_2), the precursor of sulfate aerosol,

2689   (which decrease to ~35% of 2000 levels by year 2100) and of black carbon (scaled to

2690   carbon monoxide emissions in the GFDL model) which continue to increase. This is

2691   confirmed by their respective radiative forcing values for 2100 in Table 3.6. By 2080 –

2692   2100, these projected changes in emission levels of short-lived species contribute a

2693   significant portion of the total predicted surface temperature warming for the full A1B

2694   scenario; 0.2°C in the Southern Hemisphere, 0.4°C globally, and 0.6°C in the Northern

2695   Hemisphere as shown in the time series of yearly average surface temperature change in

2696   Figure 3.9.

2697
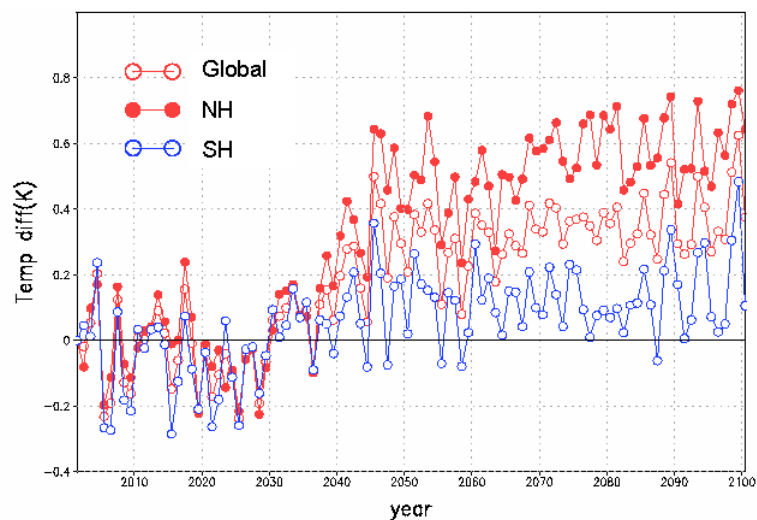
2698
2699   **Figure 3.9** Surface temperature change (2000 to 2100) due to short-lived species in the GFDL model.
2700

2701   In Figure 3.10 we examine Northern Hemisphere summer surface temperature change

2702   between the 2090s (average over 2091-2100) and the 2000s (average over 2001-2010)

2703   due to the changes in emissions of short-lived species between the first decade and the

2704   last decade of the 21st Century. Note the large warming in the Northern Hemisphere mid

2705   latitudes with the major hot spots over the continental United States, Southern Europe

2706   and the Mediterranean. Eastern Asia, the region with the strongest radiative forcing due

2707   to changes in emissions and loading of short-lived species, is not one of the hot spots.

2708   The mid latitude warm belt is statistically significant to the 95th percentile and the hottest

2709   spots are significant to the 99th percentile. By contrast, the annual-average and seasonal

2710   patterns of change in precipitation due to changes in emissions of short-lived species

2711   between the first and last decades of the 21st Century (not shown) are, in general, not

2712   statistically significant.

2713
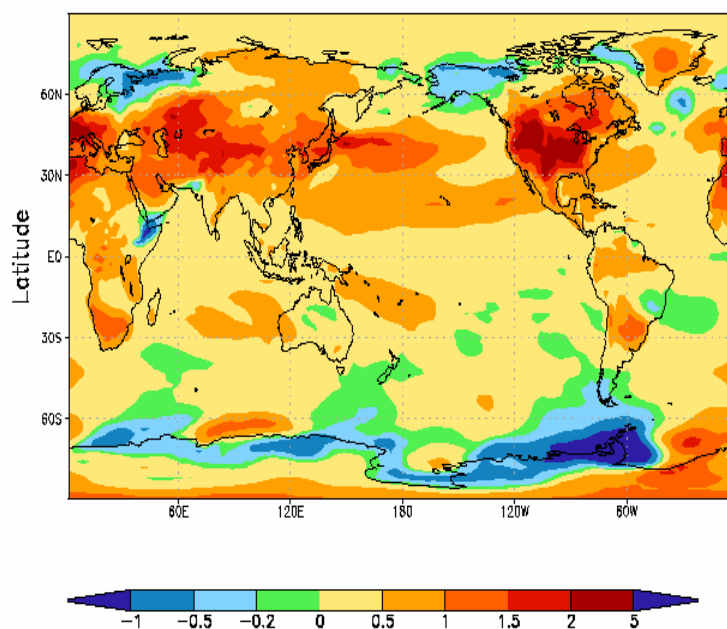
2714
2715   **Figure 3.10** Surface temperature change due to short-lived species during Northern Hemisphere summer
2716   for 2100-2091 vs. 2010-2001 in the GFDL model.
2717

2718   We now focus on the large summertime warming over the United States and consider the

2719   21st Century time series shown in Figure 3.11. By 2100, the change in short-lived species,

2720   primarily the decrease in sulfate and increase in black carbon over Asia, contribute

2721   ~1.5°C of the ~4°C temperature warming predicted for the continental United States with

2722   the effects of changes in both short-lived and long-lived species included.

2723
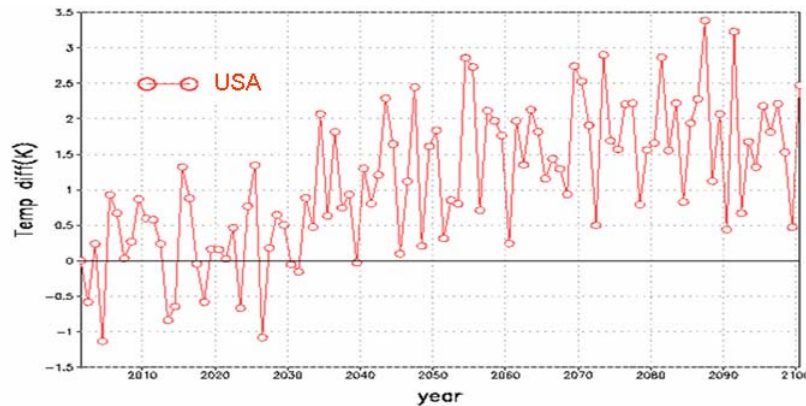
2724
2725   **Figure 3.11** Surface temperature change (K) due to short-lived species over the continental United States
2726   during Northern Hemisphere summer in the GFDL model.
2727

2728   In Figure 3.12, we focus more narrowly on the central United States where the strong

2729   summertime warming was predicted for 2100. Monthly-mean area-averaged values of

2730   temperature, precipitation, and available root-zone soil water are shown for both the full

2731   A1B emission scenario (dashed lines) and the emission scenario with short-lived species

2732   levels fixed at 2001 values (solid lines). The values are ensemble averages over the last

2733   40 years (2061-2100) for each simulation. Here the climate model does predict a

2734   statistically significant (at the 95% confidence level) decrease in precipitation due to the

2735   change in short-lived species (blue curves in Figure 3.12). We next consider root-zone

2736   soil water, a quantity that integrates and responds to both temperature and precipitation.

2737   There is a statistically significant (at the 95% confidence level) decrease of up to 50% in

2738   available root-zone soil water in the Central United States during late summer (July

2739   through September), which could have important consequences for United States grain

2740   production, and merits future attention. This is the result of a global increase in short-

2741   lived species forcing, located primarily over Asia, which in turn results from the large

2742   changes projected by the A1B "marker" scenario for Asian emissions of SO_2 and black

2743   carbon.

2744
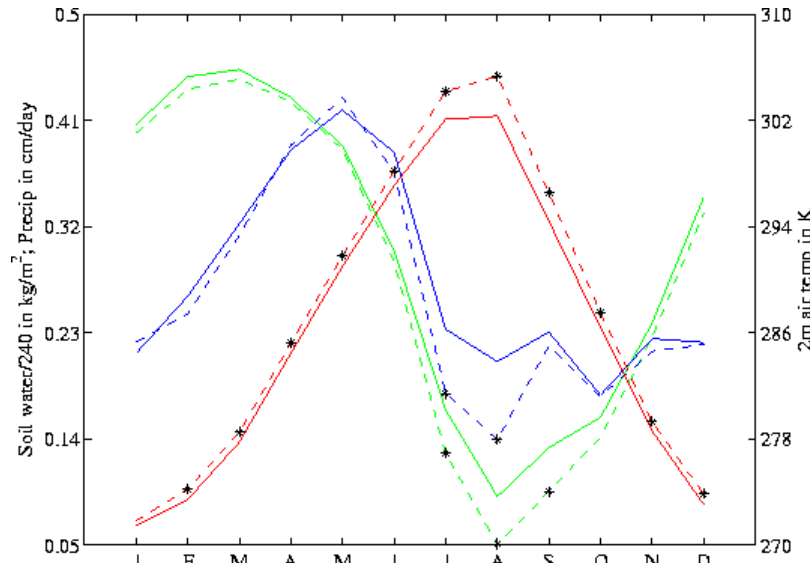
2745
2746   **Figure 3.12** Monthly-mean time-series of available root-zone soil water (green lines, scaled by a factor of
2747   1/240 for plotting purposes), precipitation (blue lines), and 2-meter air temperature (red lines), averaged
2748   over the Central United States (105 to 82.5°W longitude; 32.5 to 45°N latitude). Dashed lines are for the
2749   ensemble mean of the A1B experiments, averaged over the years 2061-2100; solid lines are for the
2750   ensemble mean of the A1B[*] experiments, also averaged over the years 2061-2100. The asterisks represent
2751   those A1B monthly average values that are different from their companion A1B[*] values at the 95%
2752   confidence level.
2753

2754   We also find, as already discussed for year 2050 in Section 3.3.4, that the regional

2755   patterns of climate change in 2100 due to changes in emissions of short-lived species are

2756   the result of regional patterns in the climate system's response, rather than regional

2757   patterns in radiative forcing. The global patterns of surface temperature change in 2100

2758   are similar for the short-lived species and the well-mixed greenhouse gases with the

2759   strongest surface temperature warming occurring over the summer continental US and

2760   Mediterranean and the winter Arctic, while the major change in radiative forcing is over

2761   Asia (Levy *et al.*, 2007). The predicted summertime warming over the US is greatly

2762   enhanced by projected reductions in SO_2 emissions and increased black carbon emissions

2763   and the resulting positive radiative forcings over Asia. In the A1B scenario, this is

2764   assumed to be the result of Asian decisions addressing their local and regional air quality.

2765   The integrated assessment model projections for A1B assume that SO_2 emissions will be

2766   reduced in the future in order to improve air quality, but did not explicitly project

2767   carbonaceous aerosol emissions. Scaling future carbonaceous emissions according to

2768   carbon monoxide emissions projections does not lead to similar reductions in emissions

2769   of these particulates, so that there is an issue of consistency in projecting the influence of

2770   future air quality decisions that deserves further study.

2771

2772   **3.4 Regional Emission Sector Perturbations and Regional Models**

2773   **3.4.1 Introduction to Regional Emission Sector Studies**

2774   An additional set of simulations used global models to examine the impact of individual

2775   emission sectors in specific regions on short-lived species. This study, in which the GISS

2776   and NCAR groups participated, was designed to examine the climate effects of short-

2777   lived species in a more policy-relevant way by focusing on the economic activities that

2778   could potentially be subject to regulation or reduction in usage (*e.g.* by improved

2779   efficiency). We look at reductions in total emissions from a given sector in particular

2780   regions (North America and Asia), and do not consider any changes in technology or the

2781   relative contributions within a sector. As such, these are more useful for assessing the

2782   potential impacts of reductions in total power/fuel usage rather than changes in the mix of

2783   power generation/transportation types or in emissions control technologies targeted at

2784   specific pollutants.

2785

2786   **3.4.2 Global Models**

2787   The GISS model setup for the regional emission sector perturbation experiments was the

2788   same as that used in the transient climate studies (section 3.2 and 3.3; see Appendix 3.1

2789   and 3.2, sections on Goddard Institute for Space Studies). The NCAR regional/sector

2790   perturbation simulations used the CAM-chem model (Lamarque *et al.*, 2005b), in which a

2791   updated version of the MOZART chemical transport model (Horowitz *et al.*, 2003) is

2792   embedded within the Community Atmosphere Model (CAM3, Collins *et al.*, 2006).

2793   CAM-chem has a representation of tropospheric chemistry with non-methane

2794   hydrocarbons (NMHCs) treated up to isoprene, toluene and monoterpenes. The aerosol

2795   simulation in CAM-chem includes the bulk aerosol mass of black carbon (BC,

2796   hydrophobic and hydrophilic), primary organic carbon (POA, hydrophobic and

2797   hydrophilic), secondary organic carbon (SOA), ammonium and ammonium nitrate, and

2798   sulfate aerosols. Further details on the CAM-chem model are found in Appendix 3.2 in

2799   the section on National Center for Atmospheric Research.

2800

2801   **3.4.3 Impact of Emission Sectors on Short-Lived Species**

2802   This set of experiments consisted of six simulations each reducing the present-day

2803   emissions by 30% in one sector for one region. By using present-day emissions, the

2804   results are not tied to any particular scenario. For present-day emissions, the IIASA 2000

2805   inventory, based on the 1995 EDGAR3.2 inventory extrapolated to 2000 using national

2806   and sector economic development data, was used (Dentener *et al.*, 2005), as in the GISS

2807   simulations described above. The exception to this is biomass burning emissions, which

2808   are taken from the Global Fire Emission Database (GFED) averaged over 1997-2002

2809   (Van der Werf *et al.*, 2003) with emission factors from (Andreae and Merlet, 2001) for

2810   aerosols. The regions were defined as North America (60-130°W, 25-60°N) and Asia

2811   (60-130°E, 0-50°N) and the economic sectors defined according to the IIASA inventory

2812   as the domestic sector, the surface transportation sector, and a combined industry and

2813   power sector (the NCAR model did not perform the transportation sector simulations).

2814

2815   A control run with no perturbations was also performed to allow comparison. The goal of

2816   these simulations was to calculate the radiative forcing from all the short-lived species to

2817   identify the relative contribution of the given economic sectors in these two regions. This

2818   complements prior work examining the response to a subset of the species included here

2819   (*e.g.,* Koch *et al.*, 2007; Unger *et al.*, 2007). As the forcings were expected to be small,

2820   we concentrate on simple metrics rather than the climate response. NCAR did not

2821   calculate radiative forcing, so we also use aerosol optical depth, which is a good indicator

2822   of the radiative forcing from aerosols. All simulations were 11-year runs, with analysis

2823   performed over the last 10 years.

2824

2825   The simulations were not performed using a full methane cycle, but the methane response

2826   to the imposed perturbations can be estimated by examining the changes in methane's

2827   oxidation rate. In these simulations, methane was prescribed at present-day values. Thus

2828   any change in methane oxidation is due solely to changes in the abundance of oxidizing

2829   agents. The difference in the steady-state abundance of methane that would occur as a

2830   result of this oxidation change is a simple calculation ($[CH_4]'/[CH_4] = L/L'$ for the global

2831   mean where L is the methane loss rate and the 'prime' notation indicates the adjusted

2832   amounts). Use of the model's oxidation rate in the perturbation runs fully captures spatial

2833   and seasonal variations, and thus provides an accurate estimate of the equilibrium

2834   response of methane to the emissions changes. Finally, the radiative forcing resulting

2835   from these indirect methane changes is calculated using the standard formulation

2836   (Ramaswamy *et al.*, 2001).

2837

2838   We first examine the global mean annual average radiative forcing in the GISS model

2839   from the regional perturbations and those by economic sectors (Table 3.10). The effect of

2840   the perturbations is generally larger for Asian than in North American emissions. The

2841   only radiative forcing from an individual species to exceed 10mW m^{-2} from a North

2842   American perturbation is the sulfate forcing from a reduction in industrial/power

2843   emissions. In contrast, forcings from sulfate, black carbon, organic carbon and ozone all

2844   exceed 10 mW m^{-2} in response to perturbations in developing Asia, with the largest

2845   response for reductions in black carbon when domestic emissions are reduced (-42 mW

2846   m^{-2}). The spatial pattern of the radiative forcing is also shown (Figure 3.13). The two

2847   largest net forcings are in response to changes in North American industrial/power

2848   emissions, whose forcing is positive and is dominated by reductions in forcing from

2849   sulfate, and the Asia domestic sector, whose forcing is negative and dominated by

2850   reductions in black carbon and ozone. The spatial pattern of the aerosol optical depth

2851   changes capture the bulk of the radiative forcing in these two cases (Figure 3.14 versus

2852   Figure 3.13). The sign is opposite, however, in the case of industrial/power emissions as

2853   these dominated by reflective sulfate aerosols, so decreased aerosol optical depth causes

2854   positive radiative forcing.

2855

2856   The GISS and NCAR models show very similar patterns of aerosol optical depth changes

2857   for these two perturbation experiments. For emissions reduction in the Asia domestic

2858   sector, the global mean aerosol optical depth decreases by 0.15 in the GISS model and

2859   0.13 in the NCAR model, while for the North American industrial/power sector the

2860   decreases are 0.09 and 0.13, respectively. Hence the aerosol response appears to be fairly

2861   robust across these two models. Results suggest that the calculation of radiative forcing

2862   from aerosol optical depth introduces an additional inter-model difference that is less than

2863   that from the aerosol optical depth calculation (Schulz *et al.*, 2006), so that the total inter-

2864   model variation in RF from aerosols is probably on order of 50%. Results for ozone show

2865   marked differences, however, with the response of the tropospheric ozone column in the

2866   GISS model nearly always a factor of 2-3 greater than in the NCAR model. We believe

2867   that these differences primarily reflect the inclusion of the stratosphere in the GISS

2868   model, which leads to enhanced forcing as ozone near the tropopause has a particularly

2869   large radiative impact. Hence, the ozone radiative forcing is not yet robust to inter-model

2870   differences. However, aerosols typically have a larger influence on climate than ozone, so

2871   that the net radiative forcing remains a relatively more robust quantity.

2872

2873   We also examine changes in surface pollution levels in these simulations. Changes in

2874   surface ozone are typically small, with annual average local reductions of up to about 1-

2875   1.5 ppbv in both the NCAR and GISS models in response to reduction in transportation

2876   or industrial/power emissions. These increase to levels of 1-3 ppbv during boreal

2877   summer. Both these annual and summer increases are statistically significant. Changes in

2878   particulate are larger. In most cases, substantial reduction in surface particulate

2879   concentrations result from the regional economic sector emissions reductions. This is

2880   especially so in the Asia domestic analysis, where summer sulfate concentrations are

2881   lowered by 100-250 pptv locally, and black carbon concentrations drop by 1800-2000

2882   pptv for both summer and annual averages. Smaller air quality improvements are also

2883   clear in the response to industrial/power and transportation emissions reductions in both

2884   regions. These reductions in particulate are generally quite similar in the two models,

2885   with differences of only 5-20% in most cases.

2886

2887   The analysis shows that reductions in surface transportation emissions have a net

2888   negative forcing from short-lived species in both regions, primarily due to reductions in

2889   black carbon and ozone. As these are both pollutants at the surface, reducing emissions

2890   transport offers a way to simultaneously improve human health and mitigate climate

2891   warming (though the climate impact is quite small for Asia). The total climate mitigation

2892   would of course be larger adding in the effect of reduced emissions of long-lived

2893   greenhouse gases. In contrast, industrial/power sector emissions have their largest effect

2894   on climate via short-lived species through sulfate, and hence yield a positive forcing.

2895   Thus, the net effect of changes in short-lived species to industrial/power emissions

2896   reductions will offset a portion of any climate benefit from reduced emissions of long-

2897   lived species. The domestic sector presents a more similar picture to that seen for surface

2898   transportation. The effects are substantially larger in Asia, however. Hence, reductions in

2899   domestic emissions from Asia offer another means to improve human health and mitigate

2900   warming. Note that the effects become particularly strong in Northern Hemisphere

2901   summer (Table 3.12), offering a potential path to help mitigating increased summer heat

2902   over the Northern Hemisphere continents.

2903

2904   Overall, the Asia domestic emissions offer the strongest leverage on climate via short-

2905   lived species. This is partially a result of their magnitude, and partially their occurrence at

2906   lower latitudes than North American (or European) emissions. This enhances their impact

2907   as photochemistry is faster and incoming radiation is more abundant at lower latitudes.

2908   Perturbing the Asia domestic sector in the IIASA 2000 emissions inventory used here

2909   yields a much greater effect via black carbon changes than via sulfate changes. This

2910   reflects the influence of domestic fuel usage, for which black carbon is the dominant

2911   emitted species, and hence reductions from emissions in this sector in particular seem

2912   attractive for warming mitigation. As domestic usage and emissions are extremely

2913   difficult to quantify in the developing world, further studies of this sector are especially

2914   needed to characterize the uncertainty in these emissions. The GISS and NCAR results

2915   differ in the magnitude of the aerosol optical depth change resulting from the Asia

2916   domestic sector perturbations by only 13%, and this sector/region has the largest

2917   influence in both models for both radiative forcing and surface pollution. The stronger

2918   aerosol optical depth response in the NCAR model suggests that the RF in that model

2919   might be even larger than the 50 mW m^{-2} global mean annual average seen in the GISS

2920   results.

2921

2922   Further work is required to more thoroughly characterize the robustness of these

2923   conclusions across a larger number of models, to explore the impact of aerosol indirect

2924   effects on clouds, and to examine alternative emissions scenarios considering changes in

2925   the mix of sources constituting a given sector and the influence of potential technological

2926   changes. The latter could be designed to reduce emissions of particular pollutants, while

2927   not affecting others. Our results for the radiative forcing from individual species give an

2928   idea of the potential impact of such technologies. However, we note that these

2929   technologies could also have effects on overall fuel consumption by altering the

2930   efficiency of a particular process.

2931

2932   Interestingly, both the transient climate projections and the present-day perturbations find

2933   that emissions from Asia are the most important controllers of climate trends or

2934   mitigation. Given that the RF reduction from decreases in Asia domestic emissions

2935   extends over much of the Northern Hemisphere (Figure 3.13), and the conclusion from

2936   the transient climate simulations that the climate response to short-lived species changes

2937   is not closely localized near their emissions, it seems plausible that emissions from this

2938   region may have as larger or larger an effect on other parts of the Northern Hemisphere

2939   as changes in local emissions.

2940   **Table 3.10** Radiative forcing (in mW m^{-2}) from regional emission sector perturbations in the GISS model.

| Region	Sector	Sulfate	BC	OC	Nitrate	Ozone	Methane (indirect)	All
North America	domestic	0	-3	2	1	2	1	4
	surface transportation	-3	-5	0	1	-5	4	-9
	industry/power	14	-2	-1	0	5	2	18
Asia	domestic	0	-42	13	1	-12	-2	-41
	surface transportation	2	-8	1	2	-5	7	-2
	industry/power	13	-4	0	-1	-1	5	12

2941   Perturbations are 30% reduction in emissions of all species from the indicated economic sector in the given
2942   region. Direct forcings are shown for sulfate, black carbon (BC), organic carbon (OC), nitrate, and ozone.
2943   The effect of ozone precursor species on methane is included as methane "indirect". Note that aerosol
2944   indirect effects are not included.
2945

2946   **Table 3.11** Total short-lived species radiative forcing (in mW m^{-2}) as in Table 3.10 but for summer (June-
2947   August).

Region	Sector	Total forcing
North America	domestic	6
	surface transportation	-10
	industry/power	34
Asia	domestic	-69
	surface transportation	-3
	industry/power	10

2948
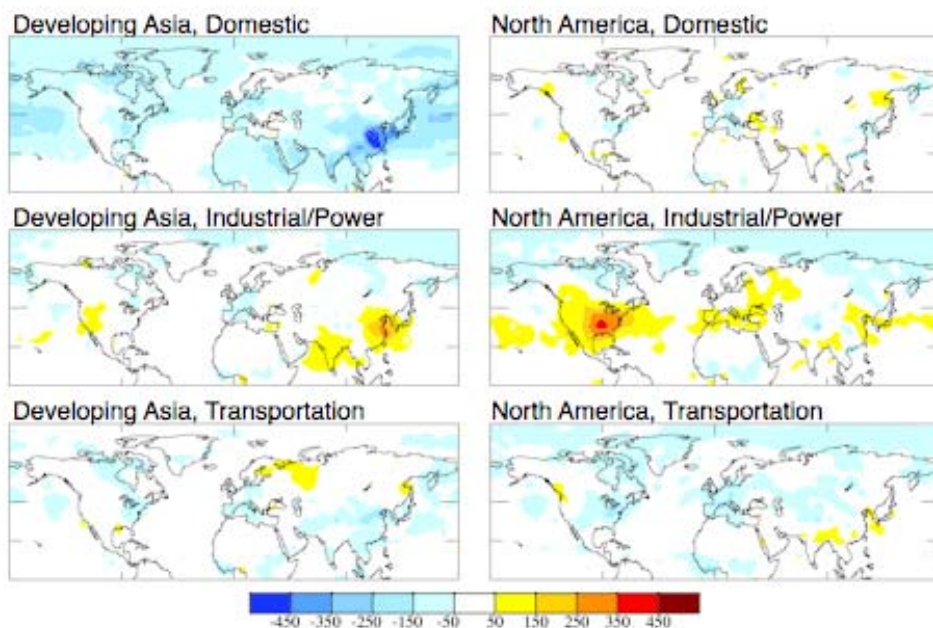
2949
2950
2951   **Figure 3.13** Short-lived species annual average radiative forcing (mW m^{-2}) due to 30% reductions in
2952   emissions from the given region and economic sector in the GISS model.
2953
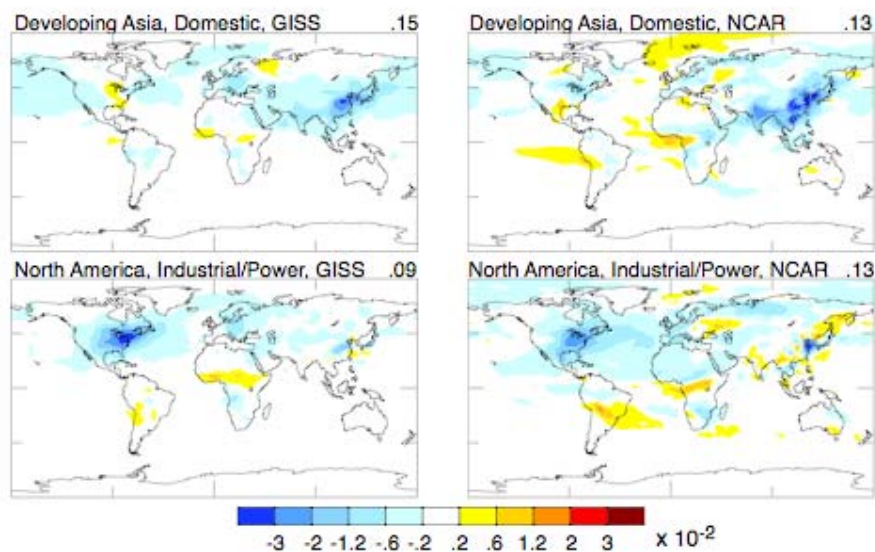
2954
2955   **Figure 3.14** Annual average aerosol optical depth change due to 30% reductions in emissions from the
2956   given region and economic sector in the GISS (left column) and NCAR (right column) models. Values in
2957   the upper right give the global mean.
2958

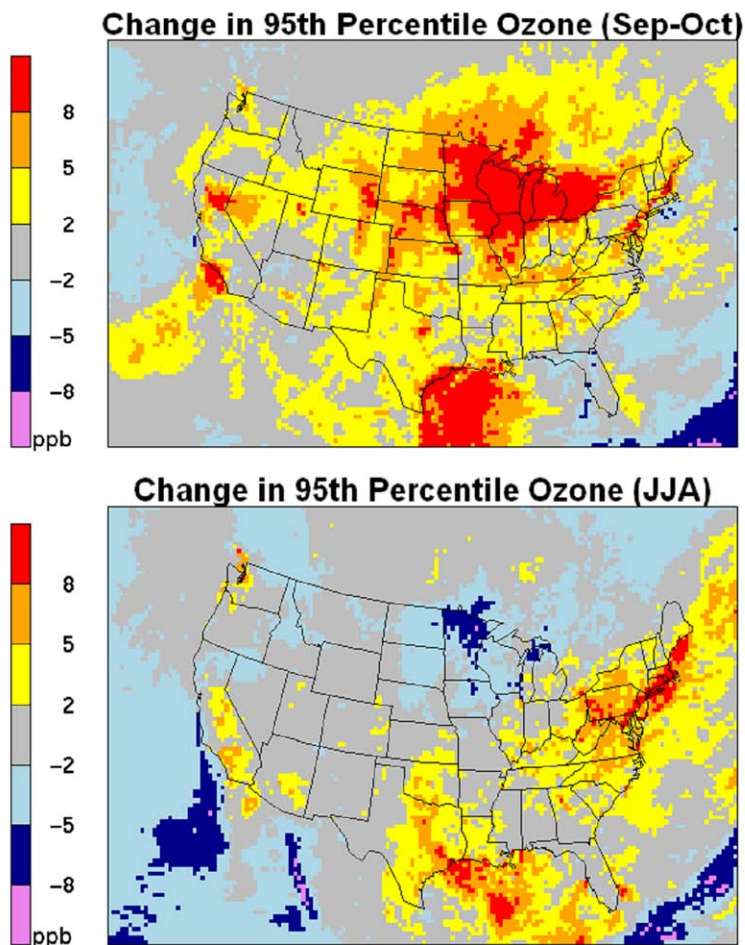2959   **3.4.4 Regional Downscaling Climate Simulations**

2960   The sector-based simulations presented in Section 3.4.3 suggest that reductions in surface

2961   level short-lived species ozone or BC would have a negative RF, while reductions in

2962   sulfate aerosols from the utility sector would have a positive RF effect. If concentration

2963   levels for these short-lived species (ozone and components of $PM_{2.5}$) exceed threshold

2964   standards under the U.S. Clean Air Act, emission control strategies must be developed.

2965   Since these short-lived species vary spatially and are affected by local emissions, regional

2966   scale models are needed to develop the emission control strategies that meet these

2967   standards at county and state levels. To achieve reductions in $PM_{2.5}$, emission scenarios

2968   often include utility sector emission reductions to lower sulfate aerosol levels. As shown

2969   in the previous section, lowering sulfate aerosol concentrations could actually have

2970   negative implications for RF and climate temperature increases. Regional downscaling

2971   studies shown in this section suggest that future changes in regional climate could reduce

2972   the benefits from anticipated emission reductions on lowering ozone.

2973

2974   Downscaled regional scale climate (RCM) simulations (*e.g.*, Leung and Gustafson, 2005;

2975   Liang *et al.*, 2006, Liang *et al.*, 2004) rely on a global climate model to provide boundary

2976   conditions for the regional domain as well as the radiative effect of well-mixed GHGs

2977   within the domain for the radiation calculations. Regionally downscaled climate

2978   simulations are needed by a number of applications that must consider local changes in

2979   future climate. Since ozone and $PM_{2.5}$ exceedances of regulatory thresholds are

2980   substantially affected by local scale changes in emissions and meteorology, several recent

2981   studies have used regionally downscaled climate scenarios have been used to study the

2982   sensitivity of air quality to potential changes in future climate. The primary purpose of

2983   these studies was to study how increases in temperature and other future climate changes

2984   could affect ozone and $PM_{2.5}$ and potentially decrease the effectiveness of anticipated

2985   emission reductions.

2986

2987   Using downscaled RCM simulations from and Gustafson (2005), Nolte *et al.* (2007) have

2988   used the EPA/NOAA CMAQ model to test the impact of future (ca. 2050) climate on

2989   ozone and aerosols with current emission scenarios. Biogenic emissions, which are

2990   meteorologically dependent, were re-calculated under the future climate scenario. Results

2991   suggest that future climate changes could increase maximum ozone levels by

2992   approximately 10% in some regions (see Figure 3.15). With anticipated emission

2993   reductions under U.S. Clean Air Act requirements, these results suggest that future

2994   climate could dampen the effectiveness of these emission controls. Evaluation of

2995   ensemble RCM results are essential for this application before quantitative conclusions

2996   can be made about the impact of future climate on specific emission control strategies;

2997   however, these results suggest that climate change is a factor that needs to be considered

2998   in air quality management.

2999

3000
3001   **Figure 3.15** From Nolte *et al.* (2007), the change in ozone at the upper end of the ozone distribution
3002   (average of the $\geq 95^{th}$ values for each grid) for (2050 - Present) years of simulation under A1B RCM
3003   simulations.
3004

3005   These regional downscaling climate studies discussed rely on climate forcing linkages

3006   from global climate simulations with future trends for long-lived species including CO_2,

3007   CH$_4$, N$_2$0, and chlorofluorocarbon. The influence of short-lived species on future climate

3008   has not been included in those studies to date; however, more recent developments are

3009   underway to include direct and indirect radiative effects in the regional chemistry model.

3010   Based on the known positive radiative forcing effect of ozone, the increases in ozone in

3011   response to future climate in Figure 3.15 should have a positive RF effect that could

3012   dampen the net negative radiative forcing anticipated from future emission reductions for

3013   ozone (see Section 3.4.3).

3014

3015   While regional downscaling climate impacts from short-lived species cannot be directly

3016   reported on, future emission scenarios for short-lived species were considered by several

3017   regional downscaling studies for the purpose of air quality impacts under future climate.

3018   The impact of climate only and then an emission change scenario were tested by (Nolte *et*

3019   *al.*, 2007) and (Hogrefe *et al.*, 2004). As presented in Figure 3.15, results looking only at

3020   the climate sensitivity without future changes in emissions suggest that future climate

3021   changes could increase maximum ozone levels by approximately 8ppb or 10% in some

3022   regions of North America. Looking at future emission scenarios for NO$_x$ and SO$_2$

3023   reductions demonstrates that the uncertainty in the future emission scenarios introduces a

3024   much larger variation in the air quality conclusions depending on the scenario (Hogrefe *et*

3025   *al.*, 2004; Nolte *et al.*, 2007). Similar to the findings here about short-lived species'

3026   impact on climate, the range of plausible air quality impacts from future short-lived

3027   emission scenarios suggest very different outcomes, and the future scenarios of emissions

3028   for short-lived species have a great deal of obvious, inherent uncertainty.

3029   **CHAPTER 3 REFERENCES**
3030
3031   **Albrecht**, B. A. (1989), Aerosols, cloud microphysics, and fractional cloudiness,
3032   Science, 245, 1227-1230.
3033
3034   **Andreae**, M. O., and P. Merlet (2001), Emission of trace gases and aerosols from
3035   biomass burning, Global Biogeochem. Cycles, 15, 955-966.
3036
3037   **Bauer**, S. E., M. I. Mishchenko, A. Lacis, S. Zhang, J. Perlwitz, and S. M. Metzger
3038   (2006), Do sulfate and nitrate coatings on mineral dust have important effects on
3039   radiative properties and climate modeling?, J. Geophys. Res., 112, D06307, doi:
3040   10.1029/2005JD006977.
3041
3042   **Berntsen** , T. K., J. S. Fuglestvedt , M. M. Joshi, K. P. Shine , N. Stuber, M. Ponater, R.
3043   Sausen, D. A. Hauglustaine, and L. Li (2005), Response of climate to regional
3044   emissions of ozone precursors: sensitivities and warming potentials, Tellus B, 57,
3045   283–304.
3046
3047   **Boer**, G., and B. Yu (2003), Climate sensitivity and response, Clim. Dyn., 20, 415-429.
3048
3049   **Bousquet**, P., *et al.* (2006), Contribution of anthropogenic and natural sources to
3050   atmospheric methane variability, Nature, 443, 439-442.
3051
3052   **Butchart**, N., *et al.* (2006), A multi-model study of climate change in the Brewer-
3053   Dobson circulation, Clim. Dyn., 10.1007/s00382-006-0162-4.
3054
3055   **Collins**, W. D., P. J. Rasch, B. E. Eaton, B. Khattatov, J.-F. Lamarque, and C. S. Zender
3056   (2001), Simulating aerosols using a chemical transport model with assimilation of
3057   satellite aerosol retrievals: Methodology for INDOEX, J. Geophys. Res., 106,
3058   7313–7336.
3059
3060   **Collins**, W. D., *et al.* (2006), The formulation and atmospheric simulation of the
3061   Community Atmosphere Model: CAM3, J. Clim., 19, 2144-2161.
3062
3063   **Delworth**, T. L., *et al.* (2006), GFDL's CM2 Global Coupled Climate Models. Part I:
3064   Formulation and simulation characteristics, J. Clim., 19, 643-674.
3065
3066   **Dentener**, F. D., D. S. Stevenson, J. Cofala, R. Mechler, M. Amann, P. Bergamaschi, F.
3067   Raes, and R. G. Derwent (2005), Tropospheric methane and ozone in the period
3068   1990-2030: CTM calculations on the role of air pollutant and methane emissions
3069   controls, Atmos. Chem. Phys., 5, 1731-1755.
3070
3071   **Dlugokencky**, E. J., S. Houweling, L. Bruhwiler, K. A. Masarie, P. M. Lang, J. B. Miller,
3072   and P. P. Tans (2003), Atmospheric methane levels off: Temporary pause or a
3073   new steady-state?, Geophys. Res. Lett., 30, 1992, doi:10.1029/2003GL018126.

3074   **Fiore**, A.M., L.W. Horowitz, E.J. Dlugokencky, and J.Jason West, Impact of
3075   Meteorology and Emissions on Methane Trends, 1990-2004 , Geophys. Res. Lett.,
3076   33, L12809, doi:10.1029/2006GL026199, 2006.
3077
3078   **Gauss**, M., *et al.* (2003), Radiative forcing in the 21st century due to ozone changes in
3079   the troposphere and the lower stratosphere, J. Geophys. Res., 108, 4292,
3080   doi:10.1029/2002JD002624.
3081
3082   **Ginoux**, P., L. W. Horowitz, V. Ramaswamy, I. V. Geogdzhayev, B. N. Holben, G.
3083   Stenchikov, and X. Tie (2006), Evaluation of aerosol distribution and optical
3084   depth in the Geophysical Fluid Dynamics Laboratory coupled model CM2.1 for
3085   present climate, J. Geophys. Res., 111, D22210, doi:10.1029/2005JD006707.
3086
3087   **Guenther**, A., *et al.* (1995), A global model of natural volatile organic compound
3088   emissions, J. Geophys. Res., 100, 8873-8892.
3089
3090   **Gustafson**, W. I., and L. R. Leung, 2007: Regional downscaling for air quality
3091   assessment: A reasonable proposition? Bulletin of the American Meteorological
3092   Society, in press.
3093   **Hansen**, J., *et al.* (2005), Efficacy of Climate Forcings, J. Geophys. Res., 110, D18104,
3094   doi:10.1029/2005JD005776.
3095
3096   **Hansen**, J., *et al.* (2007), Dangerous human-made interference with climate: A GISS
3097   modelE study, Atmos. Chem. Phys., 7, 2287-2312.
3098
3099   **Hansen**, J. E., M. Sato, and R. Reudy (1997), Radiative forcing and climate response, J.
3100   Geophys. Res., 102, 6831-6864.
3101
3102   **Held**, I. M., and B. J. Soden (2006), Robust responses of the hydrological cycle to global
3103   warming, J. Clim., in press.
3104
3105   **Hogrefe**, C., *et al.* (2004), Simulating changes in regional air pollution over the eastern
3106   United States due to changes in global and regional climate and emissions, J.
3107   Geophys. Res., 109(D22), D22301, doi:10.1029/2004JD004690.
3108
3109   **Horowitz**, L. W. (2006), Past, present, and future concentrations of tropospheric ozone
3110   and aerosols: Methodology, ozone evaluation, and sensitivity to aerosol wet
3111   removal, J. Geophys. Res., 111, D22211, doi:10.1029/2005JD006937.
3112
3113   **Horowitz**, L. W., *et al.* (2003), A global simulation of tropospheric ozone and related
3114   tracers: Description and evaluation of MOZART, version 2, J. Geophys. Res.,
3115   108(D24), 4784, doi:10.1029/2002JD002853.
3116
3117   **Kiehl**, J. T., J. J. Hack, G. B. Bonan, B. A. Boville, D. L. Williamson, and P. J. Rasch
3118   (1998), The National Center for Atmospheric Research Community Climate
3119   Model: CCM3, J. Clim., 11, 1131-1149.

3120
3121 **Kiehl**, J. T., T. L. Schneider, R. W. Portmann, and S. Solomon (1999), Climate forcing
3122   due to tropospheric and stratospheric ozone, J. Geophys. Res., 104, 31,239-
3123   231,254.
3124
3125 **Kinne**, S., *et al.* (2006), An AeroCom initial assessment – optical properties in aerosol
3126   component modules of global models, Atmos. Chem. Phys., 6, 1815-1834.
3127
3128 **Koch**, D., T. Bond, D. Streets, N. Bell, and G. R. van der Werf (2007), Global impacts of
3129   aerosols from particular source regions and sectors, J. Geophys. Res., 112,
3130   D02205, doi:10.1029/2005JD007024.
3131
3132 **Koch**, D., G. Schmidt, and C. Field (2006), Sulfur, sea salt and radionuclide aerosols in
3133   GISS ModelE, J. Geophys. Res., 111, D06206, doi:10.1029/2004JD005550.
3134
3135 **Lamarque**, J.-F., P. Hess, L. Emmons, L. Buja, W. M. Washington, and C. Granier
3136   (2005a), Tropospheric ozone evolution between 1890 and 1990, J. Geophys. Res.,
3137   110, D08304, doi:10.1029/2004JD005537.
3138
3139 **Lamarque**, J.-F., J. T. Kiehl, P. G. Hess, W. D. Collins, L. K. Emmons, P. Ginoux, C.
3140   Luo, and T. X. X. (2005b), Response of a coupled chemistry-climate model to
3141   changes in aerosol emissions: Global impact on the hydrological cycle and the
3142   tropospheric burdens of OH, ozone and NOx, Geophys. Res. Lett., 16, L16809,
3143   doi:10.1029/2005GL023419.
3144
3145 **Leung**, L. R., and W. I. Gustafson, 2005: Potential regional climate change and
3146   implications to US air quality. Geophysical Research Letters, 32, L16711,
3147   doi:10.1029/2005GL022911.
3148
3149 **Levy**, H., M. D. Schwarzkopf, L. Horowitz, and V. Ramaswamy (2007), Anthropogenic
3150   Short-lived Radiative Species at the Intersection of Climate and Air Quality,
3151   submitted.
3152
3153 **Liang**, X.Z. *et al.*, 2006: Regional climate model downscaling of the U.S. summer
3154   climate and future change. Journal Geophysical Research, in press.
3155
3156 **Liang**, X. Z., L. Li, K. E. Kunkel, M. Ting, and J. X. L. Wang, 2004: Regional climate
3157   model simulation of U.S. precipitation during 1982–2002. Part I: Annual cycle.
3158   Journal of Climate, 17(18), 3510-3529.
3159
3160 **Mahowald**, N. M., and C. Luo (2003), A less dusty future?, Geophys. Res. Lett., 30,
3161   1903, doi:10.1029/2003GL017880.
3162
3163 **Menon**, S., A. , D. Del Genio, D. Koch, and G. Tselioudis (2002), GCM Simulations of
3164   the Aerosol Indirect Effect: Sensitivity to Cloud Parameterization and Aerosol
3165   Burden, J. Atmos. Sci., 59, 692-713.

3166
3167 **Metzger**, S., F. Dentener, S. Pandis, and J. Lelieveld (2002), Gas/aerosol partitioning: 1.
3168   A computationally efficient model, J. Geophys. Res., 107,
3169   doi:10.1029/2001JD001102.
3170 **Miller**, R. L., *et al.* (2006a), Mineral Dust Aerosols in the NASA Goddard Institute for
3171   Space Studies ModelE AGCM, J. Geophys. Res., 111, D0208,
3172   doi:10.1029/2005JD005796.
3173 **Miller**, R. L., G. A. Schmidt, and D. T. Shindell (2006b), Forced variations of annular
3174   modes in the 20th century Intergovernmental Panel on Climate Change Fourth
3175   Assessment Report models, J. Geophys. Res., 111, D18101,
3176   doi:10.1029/2005JD006323.
3177
3178 **Mitchell**, J. F. B., R. A. Davis, W. J. Ingram, and C. A. Senior (1995), On Surface
3179   Temperature, Greenhouse Gases, and Aerosols: Models and Observations, J.
3180   Clim., 8, 2364–2386.
3181
3182 **Nakicenovic**, N., *et al.* (2000), IPCC Special Report on Emissions Scenarios, 570 pp.,
3183   Cambridge University Press, Cambridge, UK.
3184
3185 **Nolte**, C., A. B. Gilliland, and C. Hogrefe (2007), Linking global to regional models to
3186   investigate future climate impacts on U.S. regional air quality 1.Surface ozone
3187   concentrations, submitted.
3188
3189 **Olivier**, J. G. J., and J. J. M. Berdowski (2001), Global emissions sources and sinks, in
3190   The Climate System, edited by J. Berdowski, *et al.*, pp. 33-78, A.A. Balkema
3191   Publishers/Swets & Zeitlinger Publishers, Lisse, The Netherlands.
3192
3193 **Penner**, J. E., J. Quaas, T. Storelvmo, T. Takemura, O. Boucher, H. Guo, A. Kirkevag, J.
3194   E. Kristjansson, and Ø. Seland (2006), Model intercomparison of indirect aerosol
3195   effects, Atmos. Chem. Phys. Discuss., 6, 1579-1617.
3196
3197 **Pincus**, R., and M. Baker (1994), Precipitation, solar absorption, and albedo
3198   susceptibility in marine boundary layer clouds, Nature, 372, 250-252.
3199
3200 **Ramaswamy**, V., *et al.* (2001), Radiative forcing of climate change, in Climate Change
3201   2001, edited by J. T. Houghton, pp. 349-416, Cambridge Univ. Press, Cambridge.
3202
3203 **Schmidt**, G. A., *et al.* (2006), Present day atmospheric simulations using GISS ModelE:
3204   Comparison to in-situ, satellite and reanalysis data, J. Clim., 19, 153-192.
3205
3206 **Schulz**, M., *et al.* (2006), Radiative forcing by aerosols as derived from the AeroCom
3207   present-day and pre-industrial simulations, Atmos. Chem. Phys., 6, 5225-5246.
3208
3209 **Shindell**, D. T., G. Faluvegi, S. E. Bauer, D. M. Koch, N. Unger, S. Menon, A., R. L.
3210   Miller, G. A. Schmidt, and D. G. Streets (2007), Climate response to projected

3211   changes in short-lived species under an A1B scenario from 2000-2050 in the
3212   GISS climate model, J. Geophys. Res., 112, D20103, doi:10.1029/2007JD008753.
3213

3214 **Shindell**, D. T., G. Faluvegi, and N. Bell (2003), Preindustrial-to-present-day radiative
3215   forcing by tropospheric ozone from improved simulations with the GISS
3216   chemistry-climate GCM, Atmos. Chem. Phys., 3, 1675-1702.
3217

3218 **Shindell**, D. T., G. Faluvegi, A. Lacis, J. E. Hansen, R. Ruedy, and E. Aguilar (2006a),
3219   The role of tropospheric ozone increases in 20th century climate change, J.
3220   Geophys. Res., 111, D08302, , doi:10.1029/2005JD006348.
3221

3222 **Shindell**, D. T., G. Faluvegi, N. Unger, E. Aguilar, G. A. Schmidt, D. Koch, S. E. Bauer,
3223   and R. L. Miller (2006b), Simulations of preindustrial, present-day, and 2100
3224   conditions in the NASA GISS composition and climate model G-PUCCINI,
3225   Atmos. Chem. Phys., 6, 4427-4459.
3226

3227 **Shindell**, D. T., B. P. Walter, and G. Faluvegi (2004), Impacts of climate change on
3228   methane emissions from wetlands, Geophys. Res. Lett., 31, L21202,
3229   doi:10.1029/2004GL021009.
3230

3231 **Stevenson**, D. S., *et al.* (2006), Multi-model ensemble simulations of present-day and
3232   near-future tropospheric ozone, J. Geophys. Res., 111, D08301,
3233   doi:10.1029/2005JD006338.
3234

3235 **Stewart**, R. W., S. Hameed, and J. P. Pinto (1977), Photochemistry of the tropospheric
3236   ozone, J. Geophys. Res., 82, 3134-3140.
3237

3238 **Streets**, D., T. C. Bond, T. Lee, and C. Jang (2004), On the future of carbonaceous
3239   aerosol emissions, J. Geophys. Res., 109, doi:10.1029/2004JD004902.
3240

3241 **Tie, X.**, G. Brasseur, L. Emmons, L. Horowitz, and D. Kinnison (2001), Effects of
3242   aerosols on tropospheric oxidants: A global model study, J. Geophys. Res., 106,
3243   22931-22964.
3244

3245 **Tie, X.**, S. Madronich, S. Walters, D. P. Edwards, P. Ginoux, N. Mahowald, R. Zhang, C.
3246   Lou, and G. Brasseur (2005), Assessment of the global impact of aerosols on
3247   tropospheric oxidants, J. Geophys. Res., 110, D03204,
3248   doi:10.1029/2004JD005359.
3249

3250 **Twomey**, S. (1974), Pollution and the planetary albedo, Atmos. Env., 8, 1251-1256.
3251

3252 **Unger**, N., D. T. Shindell, D. M. Koch, and D. G. Streets (2007), Air pollution radiative
3253   forcing from specific emissions sectors at 2030, J. Geophys. Res., in press.
3254

3255 **Van der Werf,** G. R., J. T. Randerson, G. J. Collatz, and G. L. (2003), Carbon emissions
3256   from fires in tropical and subtropical ecosystems, Global Change Biology, 9, 547-
3257   562.
3258
3259 **Woodward**, S., D. L. Roberts, and R. A. Betts (2005), A simulation of the effect of
3260   climate change-induced desertification on mineral dust aerosol, Geophys. Res.
3261   Lett., 32, L18810, doi:10.1029/2005GL023482.
3262

Appendix 3.1 Composition Models

3263
3264

3265 **A.3.1.1 Geophysical Fluid Dynamics Laboratory**

3266 Composition changes for the short-lived species from 2000 to 2100 in the GFDL

3267 experiments were calculated using the global chemical transport model MOZART-2

3268 (Model for Ozone And Related chemical Tracers, version 2.4), which has been described

3269 in detail previously (Horowitz *et al.*, 2003; Horowitz, 2006; and references therein. This

3270 model was used to generate distributions of ozone, sulfate, black and organic carbon, and

3271 dust for the emission scenarios discussed in Section 3.2.1. Emissions and initial

3272 conditions for methane were scaled each decade to match the global average methane

3273 abundances specified in the A1B "marker" scenario. The model includes 63 gas-phase

3274 species, 11 aerosol and precursor species to simulate sulfate, nitrate, ammonium, and

3275 black and organic carbon and five size bins for mineral dust (diameter size bins of 0.2-2.0

3276 μm, 2.0-3.6 μm, 3.6-6.0 μm, 6.0-12.0 μm, and 12.0-20.0 μm). Hydrophobic black and

3277 organic carbon are chemically transformed into hydrophilic forms with a lifetime of 1.63

3278 days (Tie *et al.*, 2005). Different aerosol types are assumed to be externally mixed and do

3279 not interact with one another. Sulfur oxidation in the gas phase and within clouds is fully

3280 interactive with the gas-phase oxidant chemistry.

3281

3282 The transport in MOZART-2 is driven with meteorological inputs provided every three

3283 hours by the middle-atmosphere version of the NCAR Community Climate Model (Kiehl

3284 *et al.*, 1998). The meteorology was the same for each decade, thus excluding any

3285 feedbacks from climate change on natural emissions and rates of chemical reactions and

3286 removal. Thus, natural emissions, such as those of isoprene, dust, and NO_x from

3287   lightning, are held constant at present-day levels. Convective mass fluxes are re-

3288   diagnosed from the large-scale meteorology using the Hack (1994) and Zhang and

3289   McFarlane (1995) schemes. Vertical diffusion within the boundary layer is diagnosed

3290   using the scheme of Holtslag and Boville (1993). Tracer advection is performed using a

3291   flux-form semi-Lagrangian scheme (Lin and Rood, 1996).

3292

3293   The horizontal resolution is 2.8° latitude x 2.8° longitude, with 34 hybrid sigma-pressure

3294   levels extending up to 4 hPa. Photolysis frequencies for clear-sky are interpolated from a

3295   pre-calculated lookup table, based on a standard radiative transfer calculation (TUV

3296   version 3.0; (Madronich and Flocke, 1998). The values are modified to account for

3297   cloudiness (Brasseur *et al.*, 1998), but do not account for effects of the simulated

3298   aerosols. Heterogeneous hydrolysis of N_2O_5 and NO_3 on aerosol surfaces occurs at a rate

3299   based on the simulated sulfate surface area, with a reaction probability   = 0.04 (Tie *et*

3300   *al.*, 2005). Stratospheric concentrations of ozone and several other long-lived gases are

3301   relaxed to present-day climatological values.

3302

3303   Dry deposition velocities for gas-phase species are calculated off-line using a resistance-

3304   in-series scheme (Wesely, 1989). Deposition velocities for aerosol species are prescribed

3305   as by Tie *et al.* (2005). Wet removal of soluble species in and below clouds is included as

3306   a first-order loss process, based on the large-scale and convective precipitation rates, as

3307   described by Horowitz *et al.* (2003). In-cloud scavenging is based on the

3308   parameterization of Giorgi and Chameides (1985), while below-cloud washout of highly

3309   soluble species follows Brasseur *et al.* (1998). For gas-phase species, the removal rate

3310   depends strongly on the temperature-dependent effective Henry's law constant. Wet

3311   deposition of soluble aerosols (sulfate, hydrophilic BC, hydrophilic OC, ammonium, and

3312   nitrate) is calculated by scaling the removal rate to that of highly-soluble HNO_3,

3313   assuming the aerosols have a first-order loss rate constant equal to 20% of that of HNO_3

3314   (Tie *et al.*, 2005). This scaling introduces a large uncertainty into the calculation of

3315   aerosol burdens. The sensitivity of model results to this scale factor is discussed below

3316   (Section 5). Wet removal of dust is calculated using the formulation of Zender *et al.*

3317   (2003), with below-cloud scavenging efficiencies of 0.02 m^2 kg^{-1} for convective and 0.04

3318 m^2 kg^{-1} for stratiform precipitation.

3319

3320   The ozone and aerosol distributions from these simulations have been evaluated by

3321   Horowitz (2006) and Ginoux *et al.* (2006), respectively. Simulated ozone concentrations

3322   agree well with present-day observations and recent trends (Horowitz, 2006). Overall, the

3323   predicted concentrations of aerosol are within a factor 2 of the observed values and have

3324   a tendency to be overestimated (Ginoux *et al.*, 2006). The annual mean surface sulfate

3325   concentrations match observed values within a factor 2 with values ranging from 0.05 µg

3326 m^{-3} in the remote marine atmosphere to 13 µg m^{-3} in polluted regions. In general, the

3327   simulated concentrations are over-predicted in summer and under-predicted in winter.

3328   Sulfate mass column and zonal mean profiles are comparable to previous studies,

3329   although the global mean burden is about 15% higher. The annual mean concentration of

3330   carbonaceous aerosols is generally overestimated in polluted regions by up to a factor of

3331   2. An exception is West Africa where other models show significant loadings of

3332   carbonaceous aerosols associated with biomass burning activities during the dry season

3333   while our results do not show any perturbation arising from such activities. The source of

3334   this discrepancy seems to be caused in part by the emission inventory in West Africa. The

3335   annual mean dust concentration at the surface agrees with the observations to within a

3336   factor 2, except over Antarctica where it is underestimated by a factor of 5.

3337

3338   The three-dimensional monthly mean distributions of ozone, black and organic carbon

3339   aerosol, and sulfate aerosol from MOZART-2 were archived from simulations for each

3340   decade from 2000 to 2100. The results from these simulations were then interpolated to

3341   intermediate years and used in the transient climate simulations. The distribution of dust

3342   from a present-day simulation in MOZART-2 was used in all years of the climate

3343   simulations.

3344

3345   **A.3.1.2 Goddard Institute for Space Studies**

3346   The configuration of the GISS composition model used here has been described in detail

3347   in (Shindell *et al.*, 2007). The composition model PUCCINI (Physical Understanding of

3348   Composition-Climate INteractions and Impacts) includes ozone and oxidant

3349   photochemistry in both the troposphere and stratosphere (*Shindell et al.*, 2006).

3350   Photochemistry includes 155 reactions. The model calculates the abundances of 51

3351   chemical species, 26 of which are transported by the model's advection scheme. It uses

3352   'lumped families' for hydrocarbons and PANs. Chemical reactions involving these

3353   surrogates are based on the similarity between the molecular bond structures within each

3354   family using the reduced chemical mechanism of (Houweling *et al.*, 1998). This

3355   mechanism is based on the Carbon Bond Mechanism-4 (CBM-4) (Gery *et al.*, 1989),

3356   modified to better represent the globally important range of conditions. The CBM-4

3357   scheme has been

3358

3359   validated extensively against smog chamber experiments and more detailed chemical

3360   schemes. This scheme was modified for use in global models by removing aromatic

3361   compounds and adding in reactions important in background conditions, including

3362   organic nitrate and organic peroxide reactions, and extending the methane oxidation

3363   chemistry. The revised scheme was then readjusted based on the more extensive Regional

3364   Atmospheric Chemistry Model (RACM) (Stockwell *et al.*, 1997), and the modified

3365   scheme includes several surrogate species designed to compensate for biases relative to

3366   the RACM mechanism. The modified scheme was shown to agree well with the detailed

3367   RACM reference mechanism over a wide range of chemical conditions including

3368   relatively pristine environments (Houweling *et al.*, 1998).

3369

3370   Rate coefficients are taken from the NASA JPL 2000 handbook (Sander *et al.*, 2000).

3371   Photolysis rates are calculated using the Fast-J2 scheme (Bian and Prather, 2002), except

3372   for the photolysis of water and nitric oxide (NO) in the Schumann-Runge bands, which

3373   are parameterized according to (Nicolet, 1984; Nicolet and Cieslik, 1980). The aerosols

3374   component simulates sulfate, carbonaceous and sea-salt aerosols (Koch *et al.*, 2007; Koch

3375   *et al.*, 2006) and nitrate aerosols (Bauer *et al.*, 2006). It includes prognostic simulations

3376   of DMS, MSA, SO_2 and sulfate mass distributions. The mineral dust aerosol model

3377   transports four different sizes classes of dust particles with radii between 0.1-1, 1-2, 2-4,

3378   and 4-8 microns (Miller *et al.*, 2006). Most importantly, these components interact with

3379   one another, with linkages including oxidants affecting sulfate, gas-phase nitrogen

3380   species affecting nitrate, sulfate affecting nitrogen heterogeneous chemistry via reaction

3381   of N_2O_5 to HNO_3, and sulfate and nitrate being absorbed onto mineral dust surfaces (*i.e.*,

3382   the aerosols are internally mixed as coatings form on dust surfaces (Bauer *et al.*, 2006).

3383   The latter is described by a pseudo first-order rate coefficient which gives the net

3384   irreversible removal rate of gas-phase species to an aerosol surface. We use the uptake

3385   coefficient of 0.1 recommended from laboratory measurements (Hanisch and Crowley,

3386   2001), though this value is fairly uncertain.

3387

3388   Phase transformation and removal of soluble species is calculated using a wet deposition

3389   scheme in which soluble gases can be removed into either moist convective plumes or

3390   large-scale clouds as derived from the GCM's internal cloud scheme (Del Genio and

3391   Yao, 1993). During convection, all chemical species are transported along with the

3392   convective plumes, with scavenging of soluble species within and below cloud updrafts.

3393   In large-scale stratiform clouds, soluble gases are removed based on the fraction of the

3394   grid box over which precipitation is taking place. Washout of soluble species is

3395   calculated below precipitating clouds. In the case of either evaporation of precipitation

3396   before reaching the ground, or detrainment or evaporation from a convective updraft, the

3397   dissolved species are returned to the air. Wet chemistry calculations take place in each

3398   grid box at each time step, including the coupling with the convection scheme's

3399   entraining and nonentraining plumes (which are based on the convective instability in the

3400   particular grid box at that time), so are entirely consistent with the contemporaneous

3401   model physics. The solubility of each gas is determined by an effective Henry's Law

3402   coefficient, assuming a pH of 4.5. Surface dry deposition is calculated using a resistance-

3403   in-series model (Wesely and Hicks, 1977) coupled to a global, seasonally varying

3404   vegetation data set as given by (Chin *et al.*, 1996).

3405

3406   The 2000 simulation uses the 2000 emission inventory of the International Institute for

3407   Applied Systems Analysis (IIASA), except for biomass burning which is taken from the

3408   Global Fire Emission Database (GFED) averaged over 1997-2002 (Van der Werf *et al.*,

3409   2003) with emission factors from (Andrae and Merlet, 2001) for aerosols. The IIASA

3410   inventory is based on the 1995 EDGAR3.2 inventory (Olivier and Berdowski, 2001),

3411   extrapolated to 2000 using national and sector economic development data (Dentener *et

3412   al.*, 2005). Lightning NO_x emissions are calculated internally in the GCM (5.6 Tg/yr for

3413   present-day), and other natural sources are prescribed according to conventional

3414   estimates. Dust emissions are constant at 1580 Tg/yr, while isoprene emissions are 356

3415   Tg/yr. Emissions of DMS are 41 Tg/yr.

3416

3417   The simulations described here were run with this composition model included within a

3418   23-layer (up to 0.01 hPa), 4° x 5° horizontal resolution version of the ModelE climate

3419   model (Schmidt *et al.*, 2006). This composition model was used for both the transient

3420   climate and regional/sector emissions perturbation simulations.

3421

3422   Present-day composition results in the model are generally similar to those in the

3423   underlying chemistry and aerosol models documented previously. The model used here

3424   does not include the enhanced convective scavenging of insoluble species prescribed in

3425   (Koch *et al.*, 2007). Therefore our carbonaceous aerosol burden, especially in the free

3426   troposphere, is nearly double that of (Koch *et al.*, 2007). Comparison with the limited

3427   available observations is comparable between the two simulations (a positive bias

3428   replaces a negative bias).

3429

3430   **A.3.1.3 National Center for Atmospheric Research**

3431   Various methods were used at NCAR to estimate future composition. Present-day

3432   tropospheric ozone was taken from calculations performed by Lamarque *et al.* (2005)

3433   using the MOZART-2 model; beyond 2000, tropospheric ozone was calculated by T.

3434   Wigley using the MAGICC model

3435   (http://www.cru.uea.ac.uk/~mikeh/software/magicc.htm) forced by the time-varying

3436   emissions of NO_x, methane and VOCs and these average global values were used to scale

3437   the present-day distribution. Future carbonaceous aerosols were scaled from their

3438   present-day distribution (Collins *et al.*, 2001) by a globally uniform factor whose time

3439   evolution follows the global evolution of SO_2 emissions. Future levels of sulfate aerosols

3440   were calculated using the MOZART model. Stratospheric ozone changes are prescribed

3441   following the study by (Kiehl *et al.*, 1999).

3442

3443   The Model for Ozone and Related chemical Tracers version 2 (MOZART-2) is

3444   described by Horowitz *et al.* (2003) and references therein. The model provides the

3445   distribution of 80 chemical constituents (including nonmethane hydrocarbons) between

3446   the surface and the stratosphere. The model was run at a uniform horizontal resolution

3447   of ~2.8° in both latitude and longitude. The vertical discretization of the

3448   meteorological data (described below) and hence of the model consists of 18 hybrid

3449   levels from the ground to ~4 hPa. The evolution of species is calculated with a time

3450   step of 20 min.

3451   The tropospheric photolysis rates use a vertical distribution of ozone based on the

3452   simulated ozone in the troposphere and on the climatology from Kiehl *et al.* (1999)

3453   above. For each simulation, this latter distribution is updated to reflect the changes in the

3454   lower stratosphere during the 20th century, affecting only the photolysis rates and not the

3455   amount of ozone transported from the stratosphere.

3456

3457   The NCAR regional/sector perturbation simulations (Section 3.4) used a version of

3458   MOZART chemical transport model (Horowitz *et al.*, 2003) embedded within the

3459   Community Atmosphere Model (CAM3, Collins *et al.*, 2006). This model, known as

3460   CAM-chem, includes an extension of the chemical mechanism presented by Horowitz *et*

3461   *al.* (2003) to include an updated terpene oxidation scheme and a better treatment of

3462   anthropogenic non-methane hydrocarbons (NMHCs). The MOZART aerosols have been

3463   extended by Tie *et al.* (2001, 2005) to include a representation of ammonium nitrate that

3464   is dependent on the amount of sulfate and ammonia present in the air mass following the

3465   parameterization of gas/aerosol partitioning by Metzger *et al.* (2002). In brief, CAM-

3466   chem simulates the evolution of the bulk aerosol mass of black carbon (BC, hydrophobic

3467   and hydrophilic), primary organic (POA, hydrophobic and hydrophilic), second organic

3468   (SOA, linked to the gas-phase chemistry through the oxidation of atmospheric NMHCs

3469   as in (Chung and Seinfeld, 2002), ammonium and ammonium nitrate (from NH_3

3470   emissions), and sulfate aerosols (from SO_2 and DMS emissions). It also considers the

3471   uptake of N_2O_5, HO_2, NO_2, and NO_3 on aerosols. Results from the CAM-chem model are

3472   discussed by Lamarque *et al.* (2005b). A description of sea-salt, updated from Tie *et al.*

3473   (2005), is also included. Finally, a monthly-varying climatology of dust is used only for

3474   radiative calculations. The CAM-chem model considers only the direct effect of aerosols

3475   and the atmospheric model is coupled with the chemistry solely through the radiative

3476   fluxes, taking into account all radiatively active gases and aerosols. The horizontal

3477   resolution is 2° latitude x 2.5° longitude, with 26 levels ranging from the surface to ~4

3478   hPa.

3479   # Appendix 3.2 Climate Models

3480   **A.3.2.1 Geophysical Fluid Dynamics Laboratory**

3481   Climate simulations at GFDL used the coupled climate model recently developed at

3482   NOAA's Geophysical Fluid Dynamics Laboratory, which has been previously described

3483   in detail (Delworth *et al.*, 2006). We will summarize here. The model simulates

3484   atmospheric and oceanic climate and variability from the diurnal time-scale through

3485   multi-century climate change without employing flux adjustment. The control simulation

3486   has a stable, realistic climate when integrated over multiple centuries and a realistic

3487   ENSO (*Wittenberg et al.*, 2006). Its equilibrium climate response to a doubling of CO_2 is

3488   3.4C[1] (*Stouffer et al.*, 2006). There are no indirect aerosol effects included in any of the

3489   simulations. The resolution of the land and atmospheric components is 2.5° longitude x

3490   2° latitude and the atmospheric model has 24 vertical levels. The ocean resolution is 1°

3491   latitude x 1° longitude, with meridional resolution equatorward of 30° becoming

3492   progressively finer, such that the meridional resolution is 1/3° at the Equator. There are

3493   50 vertical levels in the ocean, with 22 evenly spaced levels within the top 220 m. The

3494   ocean component has poles over North America and Eurasia to avoid polar filtering.

3495

3496   Using a five member ensemble simulation of the historical climate (1861-2003) including

3497   the evolution of natural and anthropogenic forcing agents, the GFDL climate model is

3498   able to capture the global historical trend in observed surface temperature for the 20th

3499   century as well as many continental-scale features (Knutson *et al.*, 2006). However, the

3500   model shows some tendency for too much twentieth-century warming in lower latitudes

3501   and too little warming in higher latitudes. Differences in Arctic Oscillation behavior

3502   between models and observations contribute substantially to an underprediction of the

3503   observed warming over northern Asia. El Niño interactions complicate comparisons of

3504   observed and simulated temperature records for the El Chichón and Mt. Pinatubo

3505   eruptions during the early 1980s and early 1990s (Knutson *et al.*, 2006). In Figure 7d of

3506   Knutson *et al.* (2006), where the model ensemble and observations are compared grid

3507   box by grid box, ~ 60% of those grid boxes with sufficient observational data have 20th

3508   Century surface temperature trends that agree quantitatively with the model ensemble. In

3509   general, many observed continental-scale features, including a 20th century cooling over

3510   the North Atlantic, are captured by the model ensemble, as Figures 7a and 7c in Knutson

3511   *et al.* (2006) show. However, the model ensemble does not capture the observed cooling

3512   over the southeastern US and it produces a 20th century cooling over the North Pacific

3513   that is not observed.

3514

3515   **A.3.2.2 Goddard Institute for Space Studies**

3516   The GISS climate simulations were performed using GISS ModelE (Schmidt *et al.*,

3517   2006). We use a 20-layer version of the atmospheric model (up to 0.1 hPa) coupled to a

3518   dynamic ocean without flux adjustment, both run at 4 by 5 degree horizontal resolution,

3519   as in the GISS-ER IPCC AR4 simulations (Hansen *et al.*, 2007). This model has been

3520   extensively evaluated against observations (Schmidt *et al.*, 2006), and has a climate

3521   sensitivity in accord with values inferred from paleoclimate data and similar to that of

3522   mainstream GCMs; an equilibrium climate sensitivity of 2.6°C for doubled CO_2.

3523   The modeled radiatively active species influence the climate in the GCM. Ozone and

3524   aerosols can affect both the short and long wavelength radiation flux. Water uptake on

3525   aerosol surfaces influences the aerosol effective radius, refractive index and extinction

3526   efficiency as a function of wavelength and the local relative humidity (Koch *et al.*, 2007),

3527   which in turn affects the GCM's radiation field.

3528

3529   The GISS model also includes a simple parameterization for the aerosol indirect effect

3530   (Menon *et al.*, 2002) (see box on aerosol indirect effect). For the present simulations, we

3531   use only cloud cover changes (the 2nd indirect effect), with empirical coefficients

3532   selected to give roughly -1 W m^{-2} forcing from the preindustrial to the present, a value

3533   chosen to match diurnal temperature and satellite polarization measurements, as

3534   described in (Hansen *et al.*, 2005). We note, however, that this forcing is roughly twice

3535   the value of many other model studies (Penner *et al.*, 2006). The aerosol indirect effect in

3536   the model takes place only from the surface through ~570 hPa, as we only let aerosols

3537   affect liquid-phase stratus clouds.

3538

3539   **A.3.2.3 National Center for Atmospheric Research**

3540   The transient climate simulations use the NCAR Community Climate System Model

3541   CCSM3 (Collins *et al.*, 2006). This model had been run previously with evolution of

3542   short-lived species in the future for the IPCC AR4. The model was run at T85 (~1.4° x

3543   1.4° resolution). For this study, a new simulation was performed for 2000-2050 in which

3544   ozone and aerosols were kept at their 2000 levels. The equilibrium climate sensitivity of

3545   this model to doubled CO_2 is 2.7°C.

3546   **Appendix 3.2 References**
3547
3548   **Bauer**, S. E., M. I. Mishchenko, A. Lacis, S. Zhang, J. Perlwitz, and S. M. Metzger
3549   (2006), Do sulfate and nitrate coatings on mineral dust have important effects on
3550   radiative properties and climate modeling?, J. Geophys. Res., 112, D06307, doi:
3551   10.1029/2005JD006977.
3552
3553   **Bian**, H., and M. Prather (2002), Fast-J2: Accurate simulations of photolysis in global
3554   climate models, J. Atmos. Chem., 41, 281-296.
3555
3556   **Brasseur**, G. P., D. A. Hauglustaine, S. Walters, P. J. Rasch, J.-F. Müller, C. Granier,
3557   and X. Tie (1998), MOZART, a global chemical transport model for ozone and
3558   related chemical tracers, 1, Model description, J. Geophys. Res., 103, 28,265-
3559   228,289.
3560
3561   **Chin**, M., D. J. Jacob, G. M. Gardner, M. S. Forman-Fowler, P. A. Spiro, and D. L.
3562   Savoie (1996), A global three-dimensional model of tropospheric sulfate, J. Geophys.
3563   Res., 101, 18,667-618,690.
3564
3565   **Collins**, W. D., P. J. Rasch, B. E. Eaton, B. Khattatov, J.-F. Lamarque, and C. S. Zender
3566   (2001), Simulating aerosols using a chemical transport model with assimilation of
3567   satellite aerosol retrievals: Methodology for INDOEX, J. Geophys. Res., 106, 7313–
3568   7336.
3569
3570   **Collins**, W. D., *et al.* (2006), The formulation and atmospheric simulation of the
3571   Community Atmosphere Model: CAM3, J. Clim., 19, 2144-2161.
3572
3573   **Del Genio**, A. D., and M.-S. Yao (1993), Efficient cumulus parameterization for long-
3574   term climate studies: The GISS scheme, in The Representation of Cumulus
3575   Convection in Numerical Models, AMS Meteor. Monograph, edited by K. A.
3576   Emanuel and D. A. Raymond, pp. 181-184, American Meteorological Society.
3577
3578   **Delworth**, T. L., *et al.* (2006), GFDL's CM2 Global Coupled Climate Models. Part I:
3579   Formulation and simulation characteristics, J. Clim., 19, 643-674.
3580
3581   **Gery**, M. W., G. Z. Whitten, J. P. Killus, and M. C. Dodge (1989), A photochemical
3582   kinetics mechanism for urban and regional scale computer modeling, J. Geophys.
3583   Res., 94, 925-956.
3584
3585   **Ginoux**, P., L. W. Horowitz, V. Ramaswamy, I. V. Geogdzhayev, B. N. Holben, G.
3586   Stenchikov, and X. Tie (2006), Evaluation of aerosol distribution and optical depth in
3587   the Geophysical Fluid Dynamics Laboratory coupled model CM2.1 for present
3588   climate, J. Geophys. Res., 111, D22210, doi:10.1029/2005JD006707.
3589
3590   **Giorgi**, F., and W.L. Chameides (1985), The rainout parameterization in a photochemical
3591   model, J. Geophys. Res., 90, 7872-7880.

3592

3593   **Hack**, J. J. (1994), Parameterization of moist convection in the NCAR community
3594   climate model (CCM2), J. Geophys. Res., 99, 5551– 5568.

3595

3596   **Hanisch**, F., and J. N. Crowley (2001), The heterogeneous reactivity of gaseous nitric
3597   acid on authentic mineral dust samples, and on individual mineral and clay mineral
3598   components, Phys. Chem. Chem. Phys., 3, 2474-2482.

3599

3600   **Hansen**, J., *et al.* (2005), Efficacy of Climate Forcings, J. Geophys. Res., 110, D18104,
3601   doi:10.1029/2005JD005776.

3602

3603   **Hansen**, J., *et al.* (2007), Dangerous human-made interference with climate: A GISS
3604   modelE study, Atmos. Chem. Phys., 7, 2287-2312.

3605

3606   **Holtslag**, A., and B. Boville (1993), Local versus nonlocal boundary-layer diffusion in a
3607   global climate model, J. Clim., 6, 1825-1842.

3608

3609   **Horowitz**, L. W. (2006), Past, present, and future concentrations of tropospheric ozone
3610   and aerosols: Methodology, ozone evaluation, and sensitivity to aerosol wet removal,
3611   J. Geophys. Res., 111, D22211, doi:10.1029/2005JD006937.

3612

3613   **Horowitz**, L. W., *et al.* (2003), A global simulation of tropospheric ozone and related
3614   tracers: Description and evaluation of MOZART, version 2, J. Geophys. Res.,
3615   108(D24), 4784, doi:10.1029/2002JD002853.

3616

3617   **Houweling**, S., F. Dentener, and J. Lelieveld (1998), The impact of non-methane
3618   hydrocarbon compounds on tropospheric photochemistry, J. Geophys. Res., 103,
3619   10,673-610,696.

3620

3621   **Kiehl**, J. T., J. J. Hack, G. B. Bonan, B. A. Boville, D. L. Williamson, and P. J. Rasch
3622   (1998), The National Center for Atmospheric Research Community Climate Model:
3623   CCM3, J. Clim., 11, 1131-1149.

3624

3625   **Kiehl**, J. T., T. L. Schneider, R. W. Portmann, and S. Solomon (1999), Climate forcing
3626   due to tropospheric and stratospheric ozone, J. Geophys. Res., 104, 31,239-231,254.

3627

3628   **Koch**, D., T. Bond, D. Streets, N. Bell, and G. R. van der Werf (2007), Global impacts of
3629   aerosols from particular source regions and sectors, J. Geophys. Res., 112, D02205,
3630   doi:10.1029/2005JD007024.

3631

3632   **Koch**, D., G. Schmidt, and C. Field (2006), Sulfur, sea salt and radionuclide aerosols in
3633   GISS ModelE, J. Geophys. Res., 111, D06206, doi:10.1029/2004JD005550.

3634

3635   **Lamarque**, J.-F., P. Hess, L. Emmons, L. Buja, W. M. Washington, and C. Granier
3636   (2005), Tropospheric ozone evolution between 1890 and 1990, J. Geophys. Res., 110,
3637   D08304, doi:10.1029/2004JD005537.

3638
3639 **Lin**, S.-J., and R.B. Rood (1996), Multidimensional flux-form semi-lagrangian transport
3640   schemes, Mon. Wea. Rev., 124, 2046-2070.
3641
3642 **Madronich**, S., and S. Flocke (1998), The role of solar radiation in atmospheric
3643   chemistry, in Handbook of Environmental Chemistry, edited by P. Boule, pp. 1-26,
3644   Springer-Verlag, New York.
3645
3646 **Menon**, S., A. , D. Del Genio, D. Koch, and G. Tselioudis (2002), GCM Simulations of
3647   the Aerosol Indirect Effect: Sensitivity to Cloud Parameterization and Aerosol
3648   Burden, J. Atmos. Sci., 59, 692-713.
3649
3650 **Miller**, R. L., *et al.* (2006), Mineral Dust Aerosols in the NASA Goddard Institute for
3651   Space Studies ModelE AGCM, J. Geophys. Res., 111, D0208,
3652   doi:10.1029/2005JD005796.
3653
3654 **Nicolet**, M. (1984), On the photodissociation of water vapour in the mesosphere, Planet.
3655   Space Sci., 32, 871-880.
3656
3657 **Nicolet**, M., and S. Cieslik (1980), The photodissociation of nitric oxide in the
3658   mesosphere and stratosphere, Planet. Space Sci., 28, 105-115.
3659
3660 **Penner**, J. E., J. Quaas, T. Storelvmo, T. Takemura, O. Boucher, H. Guo, A. Kirkevag, J.
3661   E. Kristjansson, and Ø. Seland (2006), Model intercomparison of indirect aerosol
3662   effects, Atmos. Chem. Phys. Discuss., 6, 1579-1617.
3663
3664 **Sander**, S. P., *et al.* (2000), Chemical kinetics and photochemical data for use in
3665   stratospheric modeling, Eval. 13, JPL Publ. 00-003.
3666
3667 **Schmidt**, G. A., *et al.* (2006), Present day atmospheric simulations using GISS ModelE:
3668   Comparison to in-situ, satellite and reanalysis data, J. Clim., 19, 153-192.
3669
3670 **Shindell**, D. T., G. Faluvegi, S. E. Bauer, D. M. Koch, N. Unger, S. Menon, A., R. L.
3671   Miller, G. A. Schmidt, and D. G. Streets (2007), Climate response to projected
3672   changes in short-lived species under an A1B scenario from 2000-2050 in the GISS
3673   climate model, J. Geophys. Res., 112, D20103, doi:10.1029/2007JD008753.
3674
3675 **Shindell**, D. T., G. Faluvegi, N. Unger, E. Aguilar, G. A. Schmidt, D. Koch, S. E. Bauer,
3676   and R. L. Miller (2006), Simulations of preindustrial, present-day, and 2100
3677   conditions in the NASA GISS composition and climate model G-PUCCINI, Atmos.
3678   Chem. Phys., 6, 4427-4459.
3679
3680 **Stockwell**, W. R., F. Kirchner, M. Kuhn, and S. Seefeld (1997), A new mechanism for
3681   regional atmospheric chemistry modeling, 102, 25,847-825,879.
3682

3683   **Tie**, X., S. Madronich, S. Walters, D.P. Edwards, P. Ginoux, N. Mahowald, R. Zhang, C.
3684   Lou, and G. Brasseur (2005), Assessment of the global impact of aerosols on
3685   tropospheric oxidants, J. Geophys. Res., 110, D03204, doi:10.1029/2004JD005359.
3686
3687   **Wesely**, M.L. (1989), Parameterization of surface resistance to gaseous dry deposition in
3688   regional-scale numerical models, Atmos. Environ., 23, 1293-1304.
3689
3690   **Wesely**, M. L., and B. B. Hicks (1977), Some factors that affect the deposition rates of
3691   sulfur dioxide and similar gases on vegetation, J. Air Pollut. Control Assoc., 27,
3692   1110-1116.
3693
3694   **Zender**, C. S., H. Bian, and D. Newman (2003), Mineral Dust Entrainment and
3695   Deposition (DEAD) model: Description and 1990s dust climatology, J. Geophys.
3696   Res., 108(D14), 4416, doi:10.1029/2002JD002775.
3697
3698   **Zhang**, G.J., and N.A. McFarlane (1995), Sensitivity of climate simulations to the
3699   parameterization of cumulus convection in the Canadian Climate Centre general
3700   circulation model, Atmos. Ocean, 33, 407-446.